

Contrasting impact of irrigation on farmworker heat stress in day and night in intensely irrigated agricultural lands of California

Sagar P. Parajuli^{1*}, Trent Biggs¹, Fernando de Sales¹, Miguel Angel Zavala Perez², Cenlin He³, Charles Jones⁴, Callum Thompson⁴, Nicolas Lopez Galvez¹, Haley Ciborowski¹, Tiago Quintino⁵, Claudia Di Napoli⁵, Aliasghar Montazar⁶, Tayebbeh Hosseini Yazdi⁶, and Monica Soucier⁷

¹San Diego State University, San Diego, California

²San Diego State University Imperial Valley Campus, Calexico, California

³NSF National Center for Atmospheric Research (NCAR), Boulder, CO, USA

⁴University of California, Santa Barbara, Santa Barbara, California

⁵European Centre For Medium Range Weather Forecasts (ECMWF), UK

⁶University of California Cooperative Extension Imperial County, Holtville, California

⁷Imperial County Air Pollution Control District (APCD) Office, El Centro, California

Corresponding Author, E-mail: sparajuli@sdsu.edu

This is not a peer-reviewed research article. It is a preprint submitted to EarthArXiv. This article has been accepted for publication in Communications Earth and Environment, which can be accessed here: <https://doi.org/10.1038/s43247-024-01959-7>

Abstract

Farmworkers, the ‘frontline workers’ of our food system, are often exposed to heat stress that is likely to increase in frequency and severity due to climate change. Irrigation can exacerbate heat stress, quantification of which is crucial in intensely irrigated agricultural lands such as the Imperial Valley (IV) in southern California. We present high-resolution maps of wet bulb globe temperature (WBGT), a key indicator of heat exposure in humans, over the IV and quantify the impact of irrigation during day and night in agricultural and urban settings. We derive WBGT from a high-resolution regional climate model (WRF), which shows robust performance against station-derived WBGT metrics yielding R-square up to 0.95 and RMSE as low as 0.71 °C in agricultural sites. We find that irrigation reduces WBGT by 0.3-1.3 °C during the wet season in the daytime due to strong evaporative cooling. However, during dry season, irrigation increases WBGT by 0.4-1.3 °C at night, when the large increase in humidity sufficiently raises the wet-bulb temperature (WBT) with added increase in dry-bulb temperature (DBT) and black globe temperature (BGT), surpassing the weaker evaporative cooling. We also find that the urban and fallow areas adjacent to the crop fields experience increased heat stress due to moisture advection. Modeled WBGT frequently exceeds the regulatory threshold of 24.4 °C in the crop fields during key harvest seasons with exceedances greater than 50, 150, and 300 hours in April, June, and August 2020, respectively. The heat stress modeling framework presented serves as a prototype to develop climate change adaptation strategies for the agricultural regions of the Imperial Valley as well as the broader Central Valley and inform labor and environmental policies in California and elsewhere.

Introduction

Human heat stress is a critical public health concern globally, especially for farmworkers in hot and arid regions, and is likely to increase in frequency and severity, given recent and projected increase in global warming and heat waves¹⁻⁴. Outdoor workers, including those in agriculture, construction, and landscaping, are at special risk of exposure in the United States⁵ and globally⁶. Extreme heat stress can cause heat cramps, heat rashes, fainting, muscle rupture⁷, kidney dysfunction^{8,9}, and death due to heat strokes¹. Despite regulations at State and Federal levels, farmworkers are at high risk of heat related illnesses^{10,11}, partly due to lack of heat-related knowledge and practices among farmworkers¹². Heat stress limits are frequently exceeded in the agricultural fields of the United States^{13,14} and Mexico¹⁵.

Land cover impacts near-surface climate and heat stress exposure at local scales, due to the urban heat island effect¹⁶⁻¹⁸ and reduced air temperatures in irrigated areas^{19,20}. Irrigation impacts local climate by increasing evapotranspiration (ET)²¹, which decreases sensible heat flux and increases latent heat fluxes²⁰, and by increasing the soil heat capacity and thermal conductivity²². Irrigation can either increase or decrease human heat stress, since irrigation decreases air temperature, but also increases humidity^{20,23}. Most global and regional climate model simulations do not generally include the effect of irrigation²⁴; even if they do, the effect may be unrealistic at their coarse spatiotemporal resolution. Therefore high-resolution simulation is crucial in irrigated lands. Some previous studies have quantified the effect of irrigation on temperature globally^{24,25} at a coarse spatial resolution. A few works have also studied the impact of irrigation on heat stress on a regional scale, in California²⁶, India^{20,27}, and China, but still at coarse spatial resolution^{19,20,27}. Accurate evaluation of the effect of irrigation on a regional scale is critical because coarse-resolution simulations without irrigation tend to have systematic biases in near-surface atmospheric fields^{25,28,29}. Therefore, in this work, we mainly focus on accurately quantifying the effect of irrigation on temperature and heat stress using a well-validated regional climate model in the crop fields of the Imperial Valley (IV), California, one of the largest and most productive agricultural regions of California, where irrigation is heavily applied.

Our focus on Imperial Valley is particularly valuable because in addition to the heavy irrigation and intensive outdoor labor, this region is also characterized by a significant positive relation between soil moisture and wet-bulb temperature (WBT) and thus heat stress amplification by irrigation is more likely³⁰. Most previous studies focused on the cooling effects of irrigation on dry-bulb temperature (DBT)^{24,31}. Others have also found irrigation or soil moisture to amplify WBT^{23,30,32}. However, neither DBT nor WBT is a good heat stress metric. The former excludes the effects of humidity, while the latter depends heavily on humidity, and neither includes radiation or wind. The heat index (HI)²⁶ also does not contain radiation or wind. One of our objectives is also to re-examine irrigation impact on heat stress using the wet bulb globe temperature (WBGT).

Several indices are used to quantify heat stress^{33,34}, all of which agree on the amplification of heat stress by high humidity but disagree on the importance of humidity³⁵. Although there is no consensus around which heat index is the most robust in indicating heat stress, WBGT has become an occupational international standard in current practice^{36,37}. Unlike other simple heat

stress indices that typically include the effect of air temperature and humidity only, such as HI, WBGT additionally considers the effect of solar and thermal radiation and wind speed, and thus provides a more reliable measure of heat stress in outdoor environments. WBGT was first adopted by the US Army, after 600 heat casualties occurred in Marine Corps Recruit Depot (MCRD), Parris Island (South Carolina) in the summer of 1952^{38,39}. After the adoption of WBGT to monitor heat stress during training, the heat-related casualties decreased by five to tenfold³⁸. Although HI has been more commonly used to forecast heatwaves in the US in the past, the National Weather Service (NWS) has recently started using WBGT as an experimental product. With the rising number of heat waves in the US in recent periods, heat related regulations are rapidly changing at both federal and state levels. The NWS has recently also launched a tool called HeatRisk⁴⁰ to provide a 7-day forecast of heat risk in a color-coded index from 0 to 4. The California Office of Environmental Health Hazard Assessment (OEHHA) is also working on another similar heat index called CalHeatScore⁴¹ to provide more localized heat forecasts while accounting for health effects, in response to the requirements set by Assembly Bill No. 2238⁴². The federal Occupational Safety and Health Administration (OSHA) has recently proposed a new rule on heat injury and illness prevention that requires employers to use either HI or WBGT to determine access to shades and rest periods for employees. With these changes, Cal/OSHA is also expected to change its heat illness standard in Title 8, Section 3395 of California Code of Regulations (T8 §3395 CCR)⁴³, which uses air temperature alone to specify heat safety protocols in the Agriculture and Construction industry⁴³.

Feasibility of calculating WBGT from climate models has been demonstrated recently⁴⁴, however, at a coarse spatial resolution ($1^\circ \times 1^\circ$). The Weather Research and Forecasting (WRF) model is a widely used regional climate model for both research⁴⁵ and operational weather forecasting⁴⁶. Although WRF has been used to model WBGT indirectly in select urban region⁴⁷, it has not yet been directly used for heat stress modeling, particularly in the United States, or in regions with both irrigated agriculture and urban areas.

Previous studies have measured WBGT in agricultural regions through field surveys^{10,11,48-51}. However, a regional assessment of heat stress at the field scale using WBGT has not been done in California or in the US⁵². Regional climate models like WRF provide all parameters needed to calculate WBGT such as air temperature, humidity, and radiation fields, and at spatiotemporal scales relevant for management and policy. Numerous papers have assessed heat stress under projected climate-change scenarios, at coarse resolution on global scales⁵³⁻⁵⁷, and more recently using WBGT at ~ 5 km, daily resolution, as part of CMIP6 project⁵⁸, all of which use either HI or simplified empirical expressions for WBGT. Attempts have also been made to map heat stress at high spatial resolution in California using simple heat indices with remote sensing⁵⁹ as well as regional climate modeling^{60,61}, but not with WBGT. One key reason why WBGT is not widely used in climate projections or has been inaccurately modeled is because of the unavailability of radiation components in climate datasets.

The WBGT for outdoor environment is given by the following equation^{39,62},

$$\text{WBGT} = 0.7 \times \text{WBT} + 0.2 \times \text{BGT} + 0.1 \times \text{DBT} \quad (1)$$

where WBT is the natural wet-bulb temperature, typically measured by a ‘wet-bulb’ thermometer, BGT is the black globe temperature (or simply globe temperature) measured by a black-globe thermometer, and DBT is the dry-bulb temperature (or simply air temperature measured in weather stations).

The WBGT evolved from its predecessor, Effective Temperature, in search of simpler heat stress metrics. The weights of the WBGT equation were initially determined to closely approximate the Effective Temperature but they have been subsequently evaluated rigorously in military settings⁶². Although WBT has the largest weight in calculating WBGT (70%), BGT (20%) has substantially larger dynamic range than WBT so both components can have a significant influence on WBGT⁶³. For example, the evaluation of WBGT during 27 Army training exercises over three summer months at Quantico, Virginia showed that the BGT alone explained 59% of the variation, with WBT explaining only 17% variation³⁹.

Although WBGT is an international occupational health standard, its past use was limited to a few large institutions such as the US Army and some athletic organizations⁶⁴⁻⁶⁶. However, it is now being widely used by several other agencies, climate scientists, and weather forecasters. Still, the adoption of WBGT for heat stress monitoring remains challenging for two main reasons. First, it is difficult to measure natural WBT because it requires continuous maintenance of ‘wetting’ of a wet-bulb thermometer. In fact, commonly available WBGT measurement devices do not directly measure WBT with a ‘wet bulb’ but calculate it indirectly as a function of air temperature and humidity. Second, deployment of WBGT in large fields such as Imperial Valley (IV) farmlands is cost-prohibitive and even restrictive. Attempts have been made to calculate WBGT using commonly available data from weather stations^{63,67} as well as deriving it empirically from HI⁶⁸. A few others have incorporated solar radiation⁶⁹ (shortwave radiation) because it is also a commonly measured parameter in many weather stations. However, thermal radiation is also an important contributor of WBGT and is not typically measured in weather stations. For example, heat stress incidents can still occur on cloudy days when cumulus clouds of a passing warm front emit thermal radiation⁶². The WRF model is useful in this regard because it can provide all the parameters required for calculating WBGT, including the solar and thermal radiation. The heat stress experienced by an individual also depends on the individual’s metabolic rate^{15,70}, clothing¹⁰ and level of acclimatization⁷¹. The critical WBGT value decreases with increasing metabolic rate^{13,72}.

In this work, we use outputs from WRF including the radiation fields to calculate WBGT using the *thermofeel* python library developed by Brimicombe et al. (2023)⁷³. To our knowledge, our study is the first application of *thermofeel* for calculating WBGT in the US in an agricultural region. While the formulation of WBGT by Liljegren et al. (2008)^{74,75} has been more widely used in the US, we chose *thermofeel* for three main reasons. First, *thermofeel* is computationally more efficient than Liljegren’s approach, making it easier to implement in operational forecasting^{76,77}. A computationally more efficient formulation of Liljegren’s approach has also been recently proposed by Kong and Huber (2024)⁷⁸ for the same reason. Second, *thermofeel* was developed by the European organization European Centre for Medium-Range Weather Forecasts

(ECMWF), a trusted provider of various climate reanalysis and forecast data. Third, *thermofeel* has been validated recently and performs similarly to Liljegren’s method⁷⁶.

Given the above research gaps in measuring heat stress and the need for its continuous monitoring, we quantify WBGT at 1-km resolution using a robust, well-validated regional climate model WRF (WRF-IV) for a hyperarid irrigated area in the southwestern United States (Imperial Valley, California) (Fig. 1). Using high-resolution vegetation data and an irrigation scheme within WRF (see methods), we explore the following three research questions in this work:

1. How does irrigation change humidity, air temperature, and WBGT?
2. How accurately can WBGT be estimated using a regional climate model?
3. How often is the heat stress limit exceeded during the harvesting seasons and what are the associated policy implications?

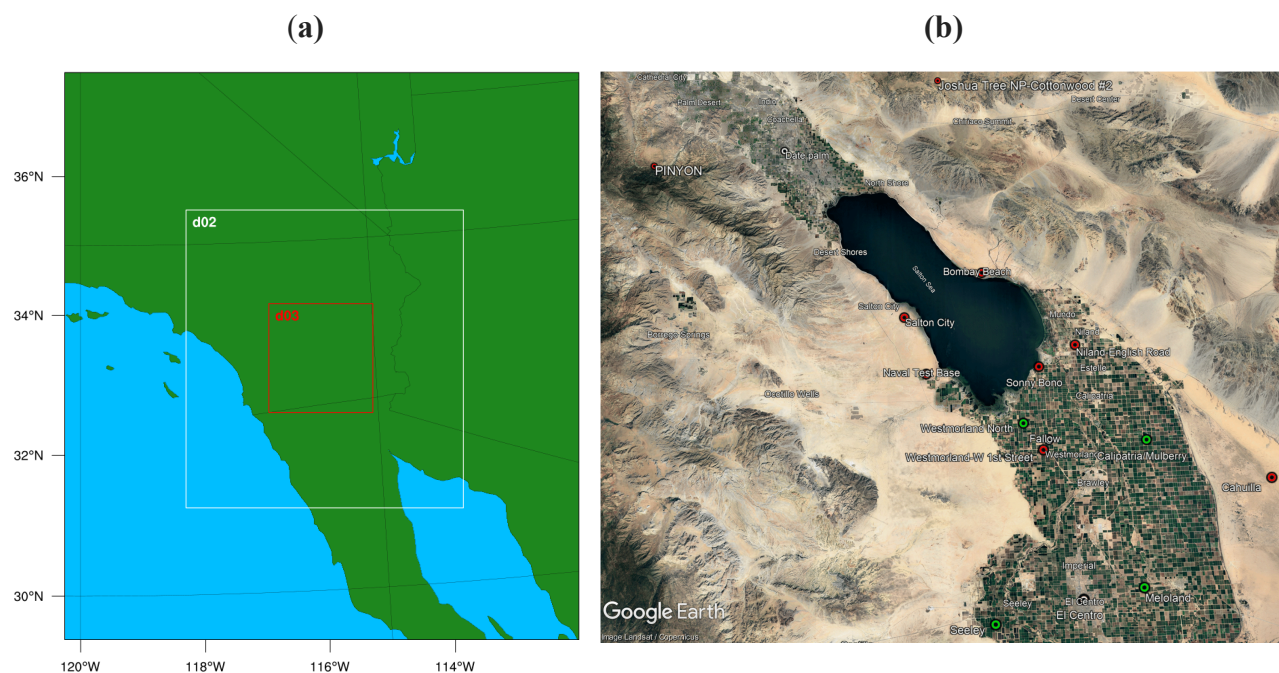


Fig. 1. (a) WRF model domain configuration showing the region of interest (d03) over the Imperial Valley and (b) the location of stations used for model validation plotted on a satellite image of the region with the Salton Sea at the center. Stations from CIMIS and CARB (Table 1) are marked with green and red circles while our recently installed stations measuring black globe temperature are marked with white circles.

Study area

The IV contains highly fertile agricultural land that produces over two-thirds of the winter vegetables such as lettuces consumed in the US⁷⁹. The All-American Canal, completed in 1942, brings about 3.3 million acre-foot of water from the Colorado River to irrigate the IV. California, mainly the Central Valley and the IV, produce over two-thirds of fruits and nuts and over

one-third of vegetables consumed in the US⁸⁰, with the labor of 829,000 individual farmworkers or 410,900 full time equivalent jobs^{48,81}. Most of the farmworkers in the IV are of Hispanic origin coming for seasonal work from the bordering town of Mexicali, Mexico¹⁰. IV has a number of socio-environmental and public health issues: about 25% of the population lives in poverty⁸², suicide is the third leading cause of death⁸³, and one in five children have asthma⁸⁴. County-level worker compensation data from 2000 to 2017 over California showed that Imperial Valley county has 36.6 heat illness rates per 100,000 workers, which is the highest in California⁸⁵.

Irrigation is critical in the IV crop fields – the average amount of irrigation applied (~ 5 ft) is more than 20 times the average annual rainfall in the region (~ 2.9 inches). Many different crops are grown in the Imperial Valley in all seasons, but not all crops have high labor requirements (e.g., alfalfa cultivation is highly mechanized) and not all seasons are critical for heat stress (e.g., winter). Based on analysis of time series of greenness from satellite imagery and discussion with farmworkers, we identify three harvesting months, which are critical from heat exposure perspectives - April, June, and August.

April has the highest greenness in the year as per the leaf area index (LAI) data in the study area (Supplementary Fig. S1). Leafy greens (lettuces), onions, and carrots are harvested in April and have high labor requirements for harvest although their planting is fully mechanized. Melons and corn are typically harvested in late spring and early summer and have high labor requirements so we also consider June in our study. Dates and grapes are harvested in summer through fall, so we also consider August. Date palms, which are typically grown in Coachella valley and northeastern IV, are typically managed and harvested in the daytime and have considerable labor requirements in different stages, e.g., trimming, netting, and harvesting. Many farmworkers migrate north to the Coachella valley in late summer for working in the vineyards and date fields (Lideres, personal communication).

Results

Model validation

Our WRF-IV model has two improvements over other regional climate models of the region: inclusion of irrigation, triggered by LAI thresholds, and updated leaf area index (LAI) data, which has higher spatial resolution of 0.5 km (Supplementary Fig. S2c) and varies for each year and month of the simulation, compared to two existing LAI datasets that are climatological averages and have coarser resolutions (10 arc-min and 30 arc-sec) typically used in WRF modeling (Supplementary Fig. S2a, b). The new LAI data resolve the spatiotemporal details of croplands and urban areas better than the existing two datasets, as shown by the difference map between new and 30 arc-sec LAI data (Supplementary Fig. S2d). For example, large solar arrays west of Calexico city (~ 32.6 N, 115.6 W, red circle) show large negative difference in LAI, indicating that these areas are erroneously assigned high LAI values in the existing LAI data, partly because these data were derived using climatological average values (2001-2010) and partly because of lower spatial resolution.

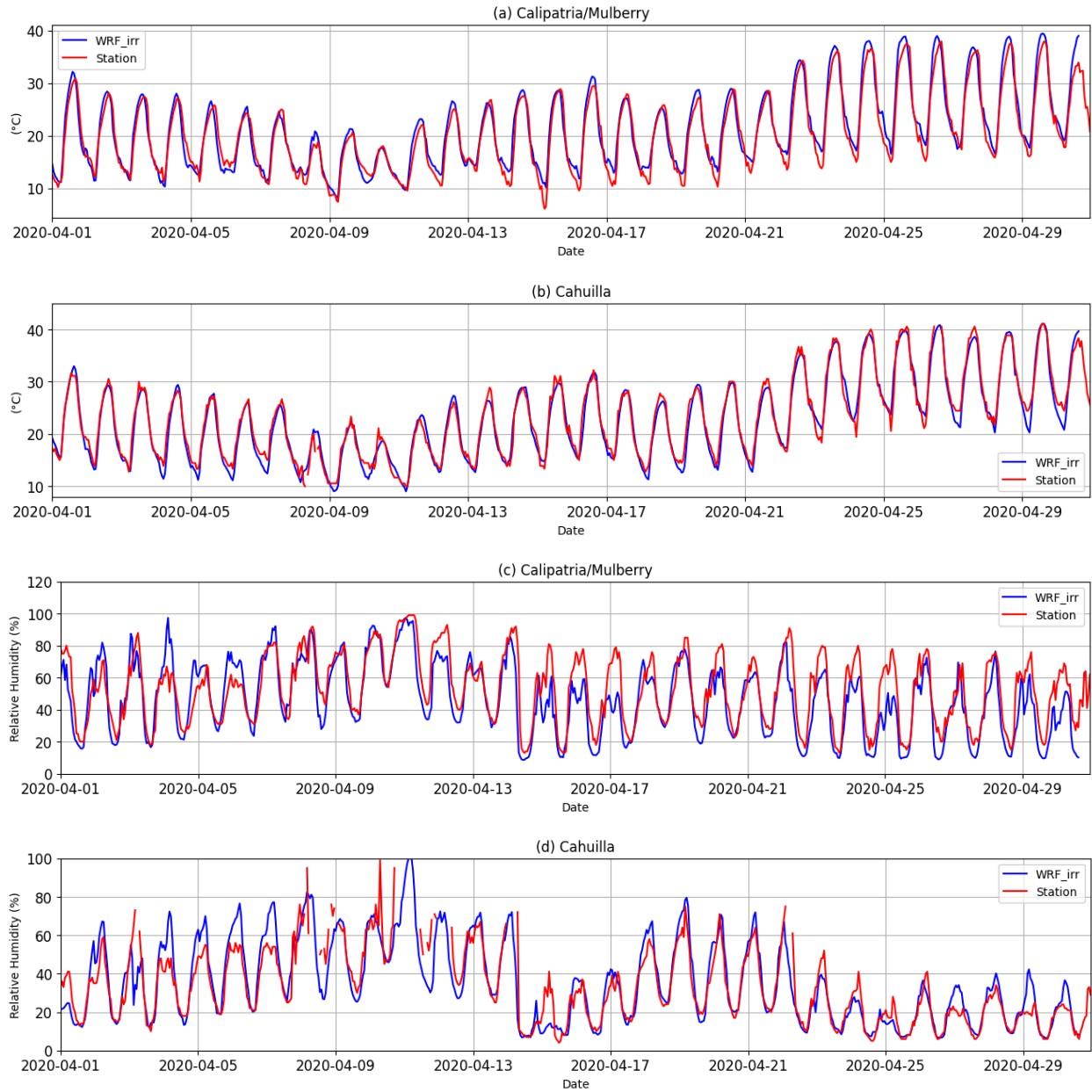


Fig. 2. Comparison of model-simulated fields with station values for representative agricultural (Calipatria) and desert (Cahuilla) stations. (a, b) 2-m air temperature (c, d) 2-m relative humidity.

The diurnal cycle of temperature and humidity is captured well by the model, as shown in the timeseries plot for representative agricultural (Calipatria/Mulberry) and desert (Cahuilla) sites (Fig. 2). The WRF-IV model shows excellent performance for temperature (Pearson's correlation coefficient (Rho) > 0.90 in all 11 sites) and good performance for relative humidity ($Rho > 0.80$ at majority of sites). Including irrigation in the model reduced air temperature and increased relative humidity compared to the non-irrigated model, reducing error and bias in both variables (Table S1). Simulated wind speed and solar radiation also show reasonable agreements with station measurements (Supplementary Table 2). Relative humidity is overestimated in the first

week of April and underestimated in some days in the later half of April. This is likely due to inadequate soil type data that did not fully resolve the variability in soil field capacity particularly when it was still raining until the first week of the month (Supplementary Fig. S3). In late April when the temperature increases sharply (Fig. 2c, d), the relative humidity is slightly underestimated.

Table 1. Statistics of model performance using meteorological stations. Rho is the Pearson correlation coefficient and RMSE is the root mean squared error.

Data source	Station	2-m air temperature		2-m relative humidity	
		Rho	RMSE	Rho	RMSE
CARB ^a	Bombay Beach (Coastal)	0.91	2.49	0.53	13.93
	Cahuilla (Desert)	0.98	1.40	0.89	9.07
	El Centro-9th Street (Urban-agricultural)	0.99	1.11	-	-
	Naval Test Base (Coastal)	0.95	2.08	0.83	9.91
	Niland-English Road (Coastal-agricultural)	0.96	1.90	0.82	11.43
	Salton City (Coastal-urban)	0.95	1.97	0.78	11.52
	Sonny Bono (Coastal-agricultural)	0.95	1.87	0.83	10.60
	Westmorland-W 1st Street (Urban-agricultural)	0.97	1.75	-	-
CIMIS ^b	Calipatria/Mulberry (Agricultural)	0.97	1.78	0.86	11.52
	Seeley (Agricultural)	0.97	1.83	0.87	9.79
	Westmorland North (Urban-agricultural)	0.96	1.98	0.79	12.41

a. California Air Resources Board

b. California Irrigation Management Information System

WBGT validation

The modeled WBGT* (see methods) values correlate closely with station-derived WBGT* values, with RMSE less than 1.28 °C for all sites and less than 0.71 °C for agricultural sites (Fig. 3, a-i). The model performance is better in agricultural or urban-agricultural sites (e.g., Calipatria, Seeley, Westmorland North, and Niland-English road) but generally weaker in stations that are located close to the Salton Sea (e.g, Sonny Bono and Salton City). This is partly because a much finer resolution simulation is required to fully resolve the exchange of heat and momentum in these coastal transition zones^{86,87}.

Comparison of modeled BGT with measured BGT data from three of our recently installed stations at Westmoreland, Coachella, and El Centro (Fig. 1) show good agreement (Fig. 3, j-l). The model performance is very good at the urban (El Centro) and agricultural sites (Westmoreland) but moderate at the date palm (Coachella) site. This is reasonable given the existence of tall date palm trees at the Coachella site, which again require much finer resolution to fully resolve the local circulation.

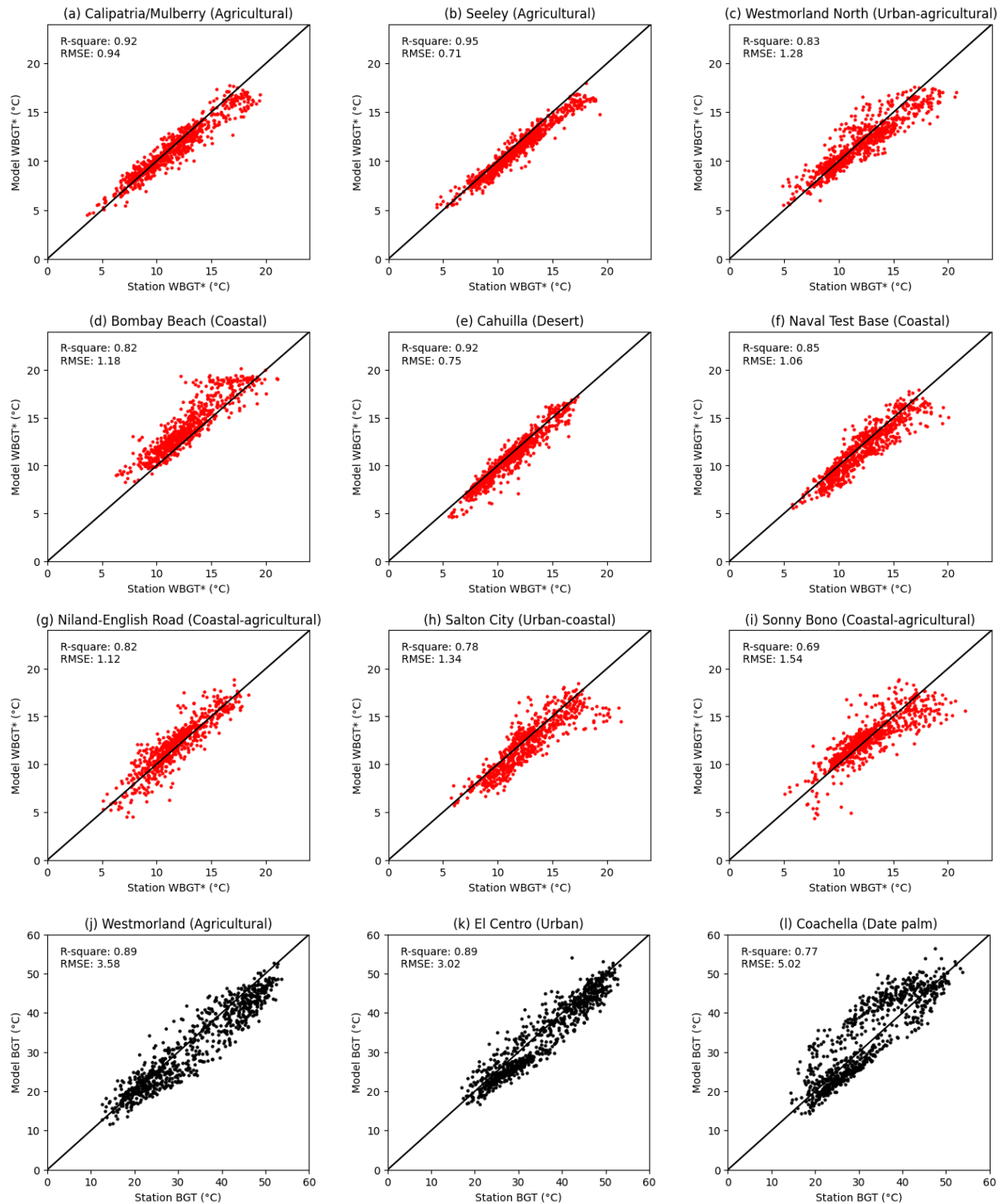


Fig. 3. Model-derived WBGT* vs. station-derived values for the period April 1-30, 2020 (a-c) CIMIS sites (d-i) CARB sites. WBGT* represents the first and third terms of the WBGT equation (eq. 1) excluding the second term. (j-l) Model-derived hourly BGT vs. station-measured BGT for a different period May 21-June 22, 2024.

Irrigation effect

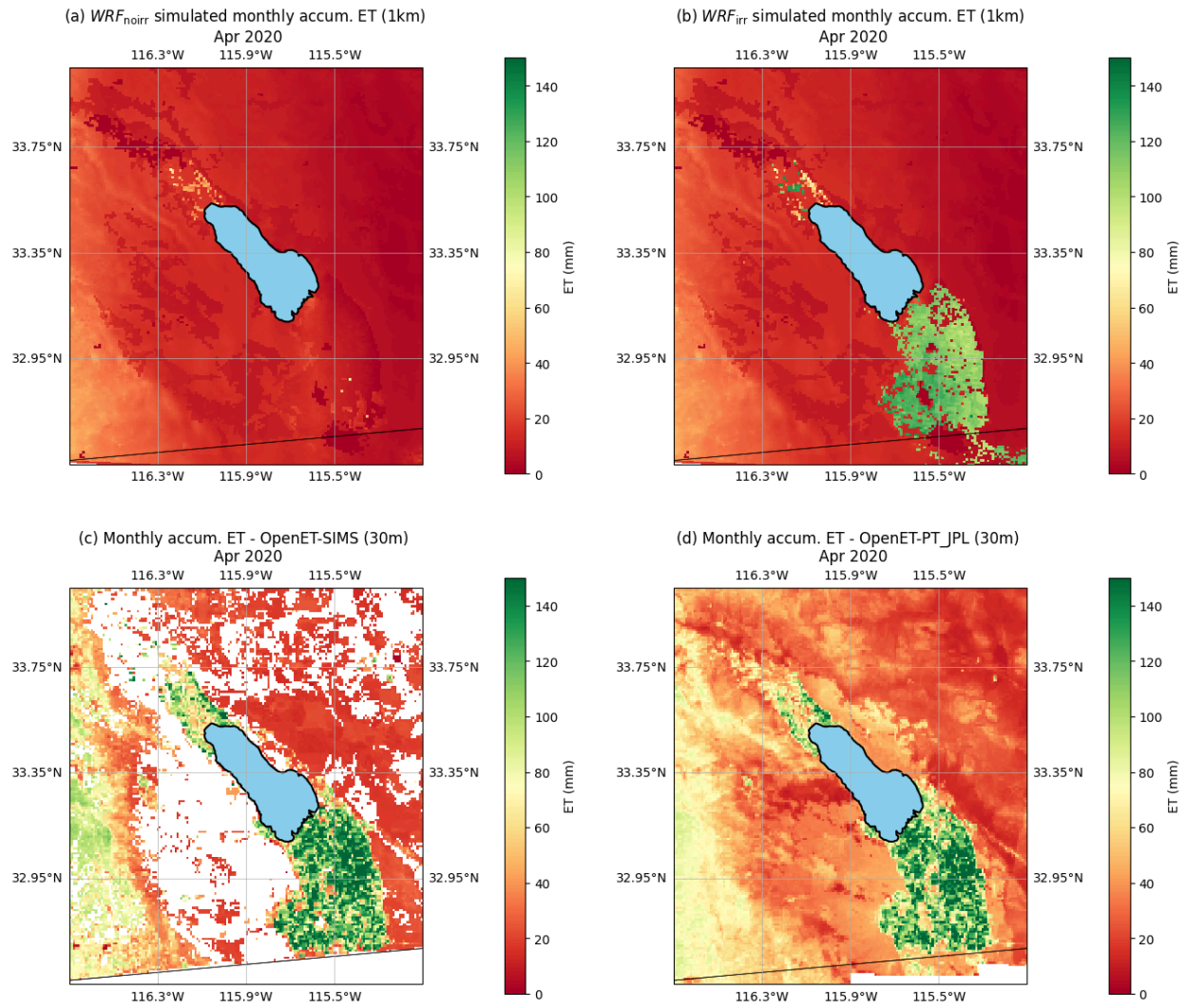


Fig. 4. Contribution of irrigation on evapotranspiration (ET). (a) ET simulated by WRF with no irrigation (b) same as (a) but with irrigation (c) ET from OpenET SIMS model (d) ET from OpenET PT-JPL model.

The model without irrigation greatly underestimates the ET in the cropped areas (compare Figs. 4a and b for April). Application of irrigation increases ET remarkably (from ~0-20 to ~100-140 mm per month) and brings it closer to the satellite-derived ET estimates (Figs. 4c, d).

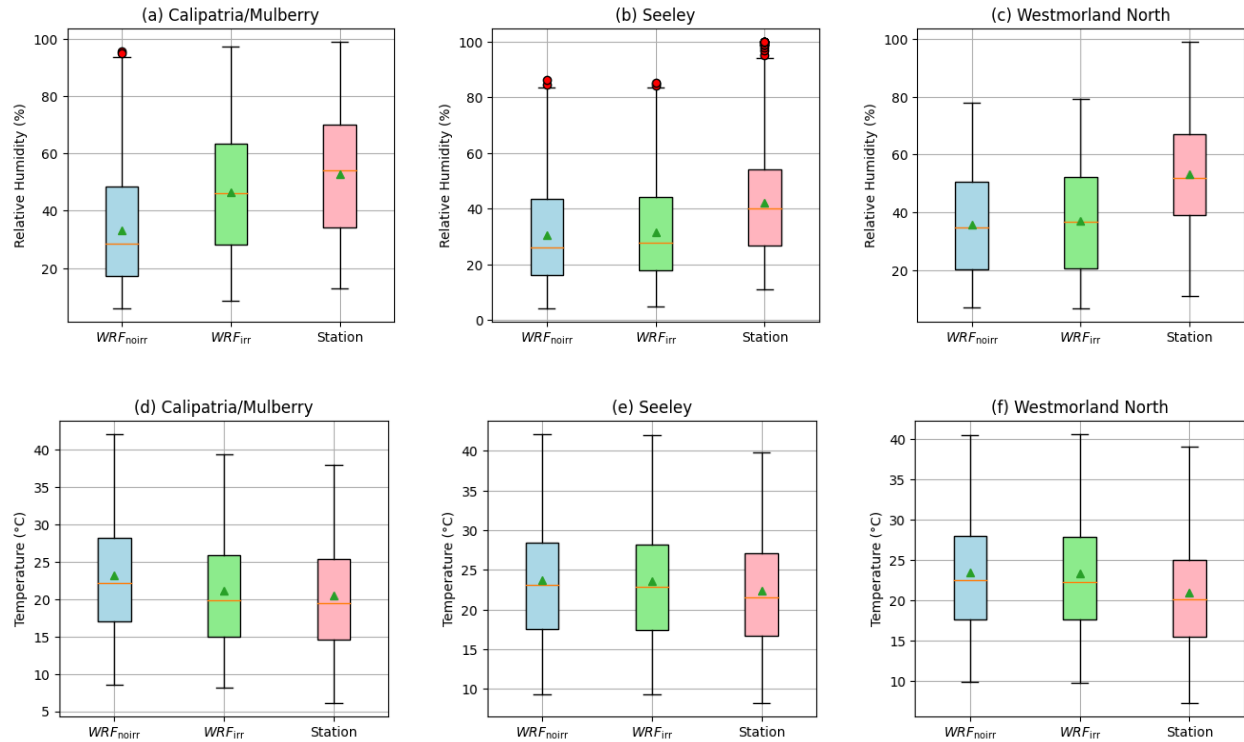


Fig. 5. Effect of irrigation on modelled humidity and temperature. Box plot for (a-c) humidity and (d-f) temperature for CIMIS sites. WRF_{noirr} and WRF_{irr} correspond to the model simulations without and with irrigation. The green triangle represents the mean, the horizontal line within the box represents the second quartile (median), the lower (upper) end of the box represents the first (third) quartile. The lower (upper) whiskers represent $(Q3-1.5 \times IQR)$ and $(Q3+1.5 \times IQR)$, respectively, where IQR is the interquartile range; the red dots represent the outliers outside this range.

Irrigation increases modeled humidity and reduces the modeled air temperature, bringing them closer to station values, which is particularly prominent at the agricultural site Calipatria (Fig. 5). Although Seeley and Westmorland North stations lie within the greater agricultural fields, they are located next to urban centers where the flow and moisture transport becomes more complex. Model error at these stations does not decrease by adding irrigation.

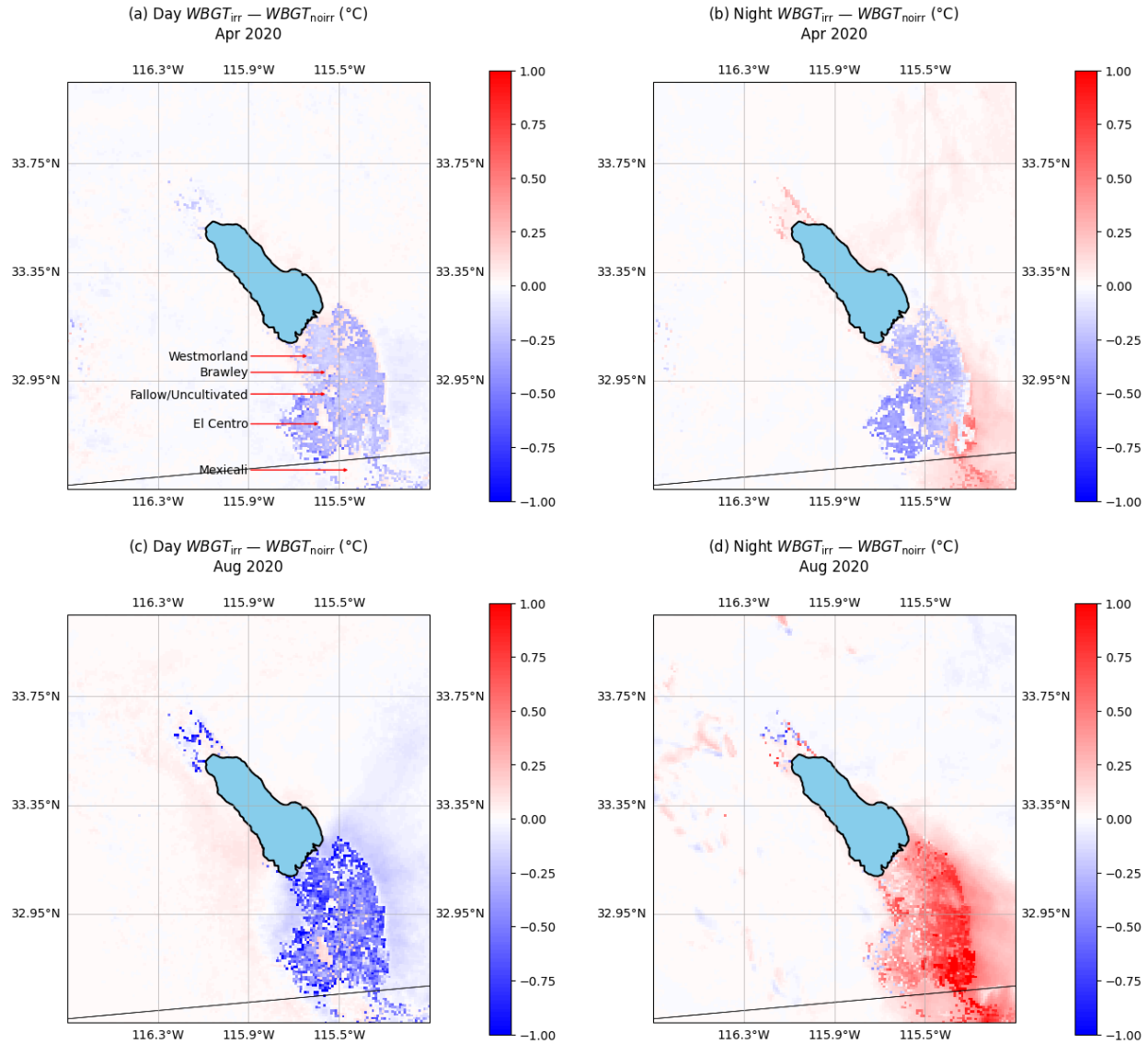


Fig. 6. Irrigation effect on WBGT in the daytime and nighttime for (a, b) April and (c, d) August, 2020. $WBGT_{noirr}$ and $WBGT_{irr}$ correspond to the model simulations without and with irrigation.

In April daytime, irrigation decreases WBGT in crop fields and slightly increases WBGT values in nearby urban areas (e.g., Westmorland, Brawley) and fallow/uncultivated fields (Fig. 6a). At night, the increase in WBGT becomes more prominent particularly in the downwind desert areas east of the IV crop fields and southeastern region including the cultivated areas east of Mexicali (Fig. 6b). In August, both effects are remarkably stronger: daytime shows strong reduction in WBGT (Fig. 6c) while nighttime shows a consistent increase in WBGT across all crop fields (Fig. 6d).

The grid cells showing a stronger (weaker) change in WBGT have lower (higher) p-values consistent with the stronger (weaker) effect of irrigation, as evaluated by difference of mean t-test (Supplementary Fig. S4). In April and August daytime, 42 and 1394 grid points ($\sim 42 \text{ km}^2$

and 1394 km^2), respectively, have statistically significant decreases in WBGT at 10% significance level, with no grid points showing significant increase in WBGT (Supplementary Fig. S5a, c). In the nighttime, 93 and 1469 grid points show significant increase in WBGT in April and August, respectively, while 190 (April) and 27 (August) grid points show significant decrease in WBGT (Fig. S5b, d). Considering only grids with statistically significant ($p < 0.1$) change, irrigation reduces monthly average WBGT by 0.4 to 0.7 °C in daytime depending upon the location and increases WBGT by 0.4 to 0.6 °C in the nighttime in spring (April). Similarly, irrigation reduces WBGT by 0.3 to 1.3 °C in spring daytime (April) and increases by 0.4 to 1.3 °C at nighttime in August.

Physical mechanisms of irrigation impact

Impacts of irrigation on WBGT is a consequence of the impact of irrigation on WBGT's three constituent terms which are DBT, WBT, and BGT. These three terms are ultimately governed by changes in underlying physical parameters such as humidity, evapotranspiration, air temperature, soil moisture, land surface temperature, and sensible/latent heat. Below we explain how irrigation impacts DBT, WBT, and BGT along with the associated physical parameters that change WBGT.

Irrigation impacts all three terms of the WBGT equation: WBT, BGT, and DBT (Fig. 7). We observed irrigation-induced reduction in BGT and DBT over most of the study area both in April and August, but some areas in the southeastern part of the domain show an increase in BGT and DBT in August nights. The similar pattern of increase in DBT and BGT in August nights indicates that they are correlated (Fig. 7). This contrasting impact of irrigation on DBT and BGT in April and August is one key factor leading to the contrasting impact of irrigation on WBGT in April and August nights.

The increase in DBT and BGT due to irrigation in August nights can be explained by the change in soil temperature or skin temperature (TSK) due to irrigation. While TSK generally decreases in most of the IV area regardless of the month, TSK increases in the areas with an increase in DBT and BGT in August nights (Fig. S9). This suggests that the increase in skin temperature increases DBT and BGT. The increased TSK increases the outgoing longwave radiation, which increases the DBT and BGT. The increase in TSK is due to increased heat capacity and thermal conductivity of the soil by irrigation, which increases energy storage during the daytime and contributes to the surface warming at night²². The reduction in TSK due to irrigation in the rest of the IV area in both day and night is consistent with previous studies¹⁹.

The widespread reduction in DBT and BGT due to irrigation is consistent in both wet (April) and dry (August) months, which can be attributed to widespread evaporative cooling of the crop fields, as demonstrated by changes in latent heat (LH). The larger increase in LH in the daytime than in the nighttime (Fig. S9) indicates stronger evaporative cooling in the daytime, which reduces DBT and BGT more strongly, ultimately causing larger reduction in WBGT in the daytime than at night (Fig. 6).

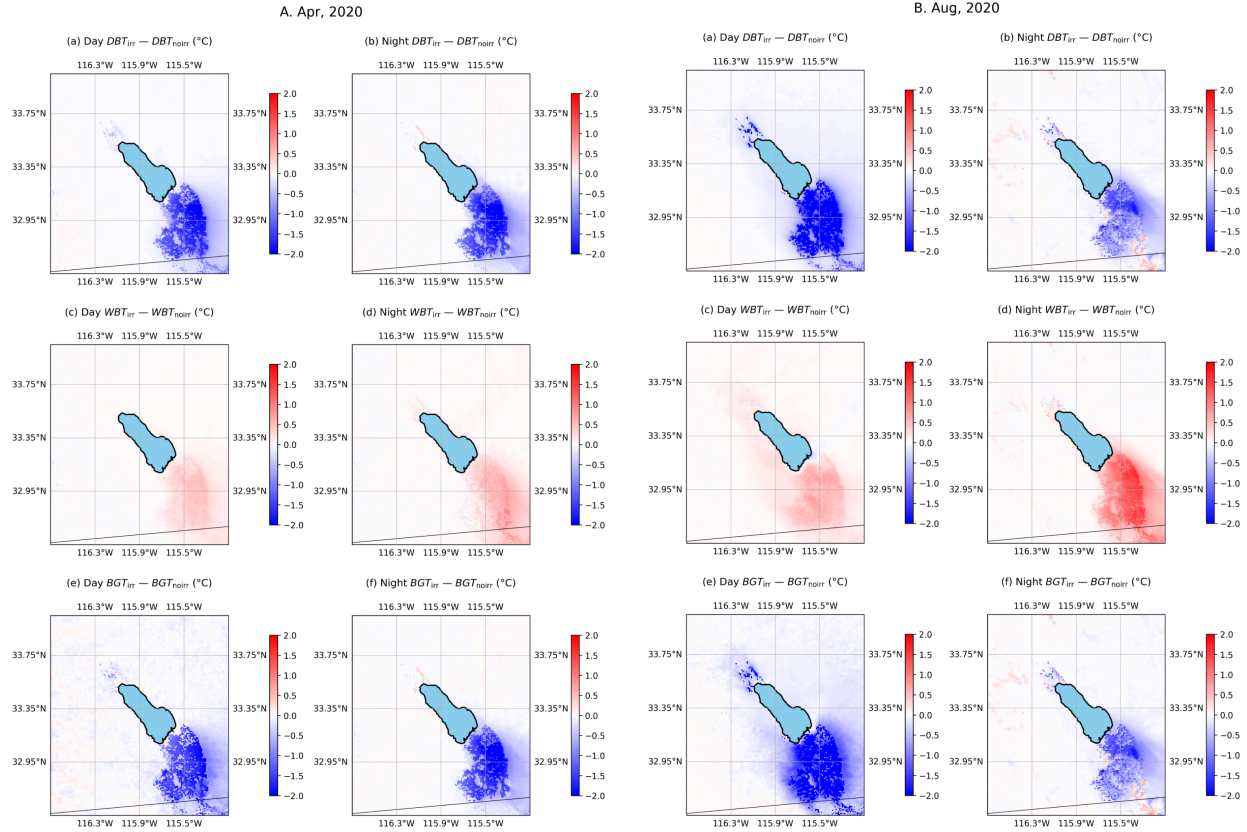


Fig. 7. Impact of irrigation on the three terms of the WBGT equation DBT, WBT, and BGT. Difference in temperatures between irrigation-on and irrigation-off simulations presented separately for daytime and nighttime for (A) April and (B) August, 2020.

Irrigation consistently increases WBT regardless of the seasons but the increase is remarkably higher in August nights (Fig. 7), another key factor for the contrasting impact of irrigation on WBGT in August and April nights (Fig. 6). This large increase in WBT in August night leads to uniform increases in WBGT in the entire IV region in contrast to April night, which shows mixed impact on WBGT due to smaller increase in WBT. The pattern of WBT changes in August nights (Fig. 7d, panel B) is also similar to that of WBGT, which indicates that the increase in WBGT is strongly governed by increase in WBT. In April nights, only the southeastern parts of the domain (Fig. 6b), where the increase in WBT is very strong (Fig. 7d, panel A), have increased WBGT with irrigation (Fig. 6a). In other cropped areas, the reduction in BGT and DBT is much stronger compared to the increase in WBT (Fig. 7), thus these areas do not show a net increase in WBGT in April nights. In August nights, the reduction in BGT and DBT due to irrigation is not as strong as in April nights (Fig. 7), thus WBGT uniformly increases across the entire domain (Fig. 6).

The increase in WBT can be explained by the increase in specific humidity due to irrigation. Irrigation has marked effects on humidity levels (Fig. 8) through the increase in evapotranspiration (Fig. 4). The increase in humidity in the model with irrigation is much larger in August (Fig. 8d) than in April (Fig. 8b), which explains why there is a larger increase in WBT

in August than in April (Fig. 7). This differential change in humidity can be attributed to the higher temperature and larger amount of irrigation water applied by the model in August (supplementary Fig. S6b) than in April (Fig. S6a). Note that the model applies different amounts of irrigation water in different grid cells to bring the current soil moisture to the field capacity. The northern IV crop fields show more irrigation applied, particularly in August (Fig. S6b), because of the lower modeled soil moisture in these areas compared to southern areas (not shown).

Atmospheric moisture advection also impacts WBGT in the study area. Pre-irrigation humidity level is higher in August than in April (compare Fig. 8a, c) due to higher moisture advection from the Salton Sea. In the nighttime, the air above the Salton Sea remains warmer than the air above the surrounding land, causing higher specific humidity levels over the Salton Sea (supplementary Fig. S7), which gets advected to the crop fields. The advected moisture gets confined to the eastern side of the cropped region because of the westerly/southwesterly downslope winds, which are stronger at night (Fig. S8). Because of higher background moisture, there is a larger increase in WBT in the eastern side of the crop fields at night (Fig. 7). We also observed a larger increase in specific humidity due to irrigation in the nighttime than in the daytime (not shown), which is consistent in both wet and dry months, which explains the larger increase in WBT at night (Fig. 7).

The sign of changes in soil moisture (SM), latent heat (LH), and sensible heat (SH) are consistent in wet (April) and dry (August) periods (Fig. S9). The SM, LH, and specific humidity increase while the SH decreases due to irrigation, consistent with previous studies^{20,27}. These results demonstrate that our results are physically plausible and consistent with the literature.

WBGT increased in the urban/fallow areas in the model with irrigation. A combination of temperature and moisture advection might have contributed to the WBGT changes in nearby urban/fallow areas. Irrigation clearly causes a cooling effect on air temperature (DBT) in the crop fields (Fig. 7, first row), so WBGT may not increase in the urban/fallow areas through temperature advection. Since 'irrigation' is only applied in the crop fields, one possible way by which the irrigation can affect the urban and fallow area is through moisture transport from the crop fields. To further ascertain this, we calculated the average increase in specific humidity in the urban/fallow areas following irrigation, by identifying the urban/fallow areas within the blue box (supplementary Fig. S6), where irrigation water applied is zero. The urban/fallow grids still experienced average increased humidity of 2.9 g kg^{-1} in the daytime and 6.3 g kg^{-1} in the nighttime of April through moisture transport, which is about 50% of the increase in cropped areas where irrigation is applied. The contrasting effect of irrigation on WBGT in crop fields and urban/fallow areas occurs in August as well (Fig. 6c, d); the overall increase/decrease in WBGT is much stronger in August than in April in response to more irrigation water applied in August (Fig. S6).

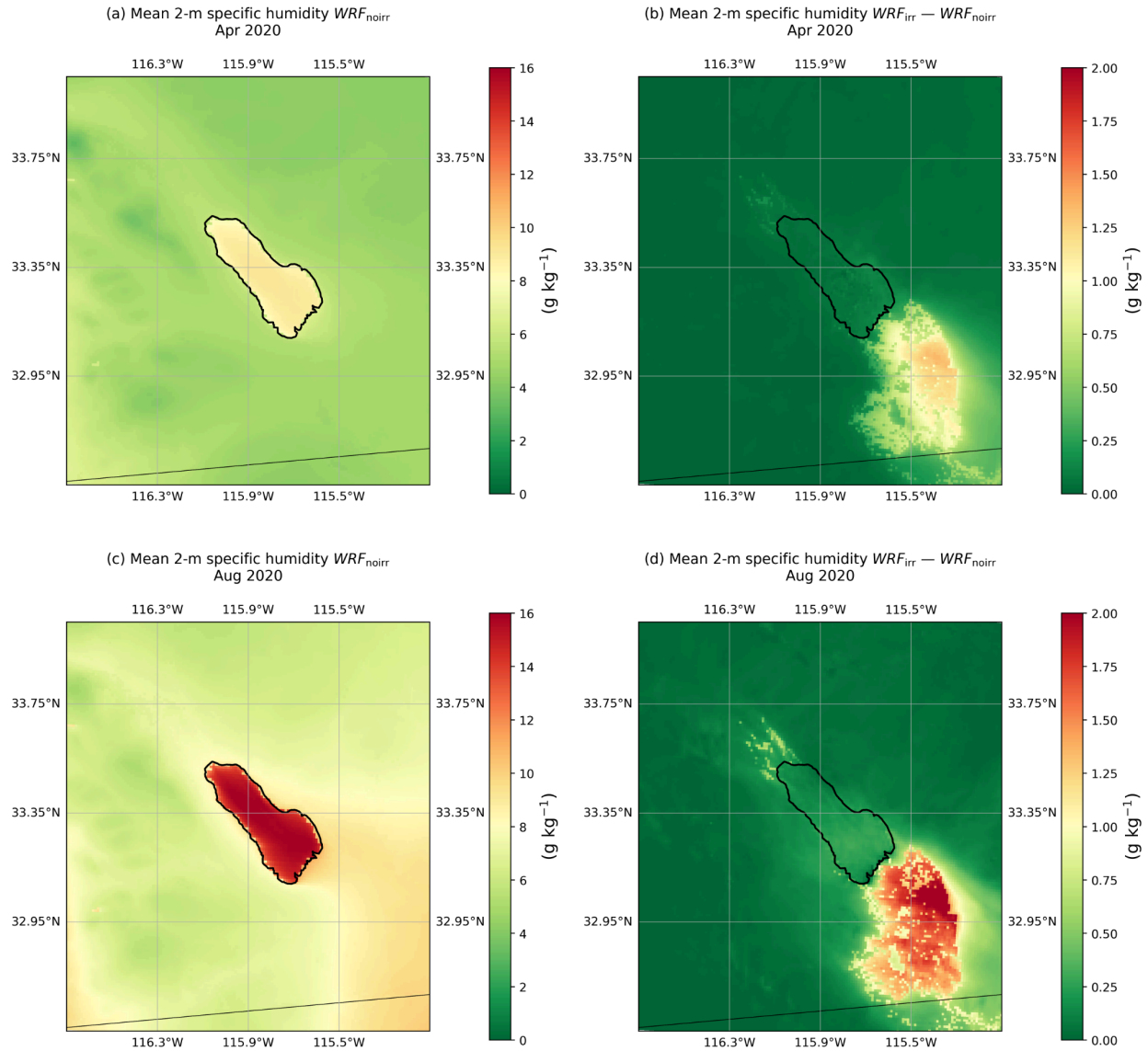


Fig. 8. Change in specific humidity due to irrigation. Mean 2-m specific humidity from WRF irrigation-off simulations for (a) April and (c) August, 2020 and the difference between irrigation-on and irrigation-off simulations for (b) April and (d) August, 2020.

In addition to the direct physical mechanisms affecting WBGT, there can be additional feedback from larger-scale atmospheric processes. For example, the cooling of the crop fields can reduce the boundary layer height²⁰, which restricts mixing in the boundary layer consequently warming the near surface air temperature. A more in-depth exploration of the underlying physical mechanisms by which irrigation impacts WBGT is out of the scope of this study. The contrasting physical mechanisms by which irrigation increases or decreases WBGT, in crop fields and urban/fallow areas, and in day and night time, are summarized in the accompanied schematic diagram (Fig. 9).

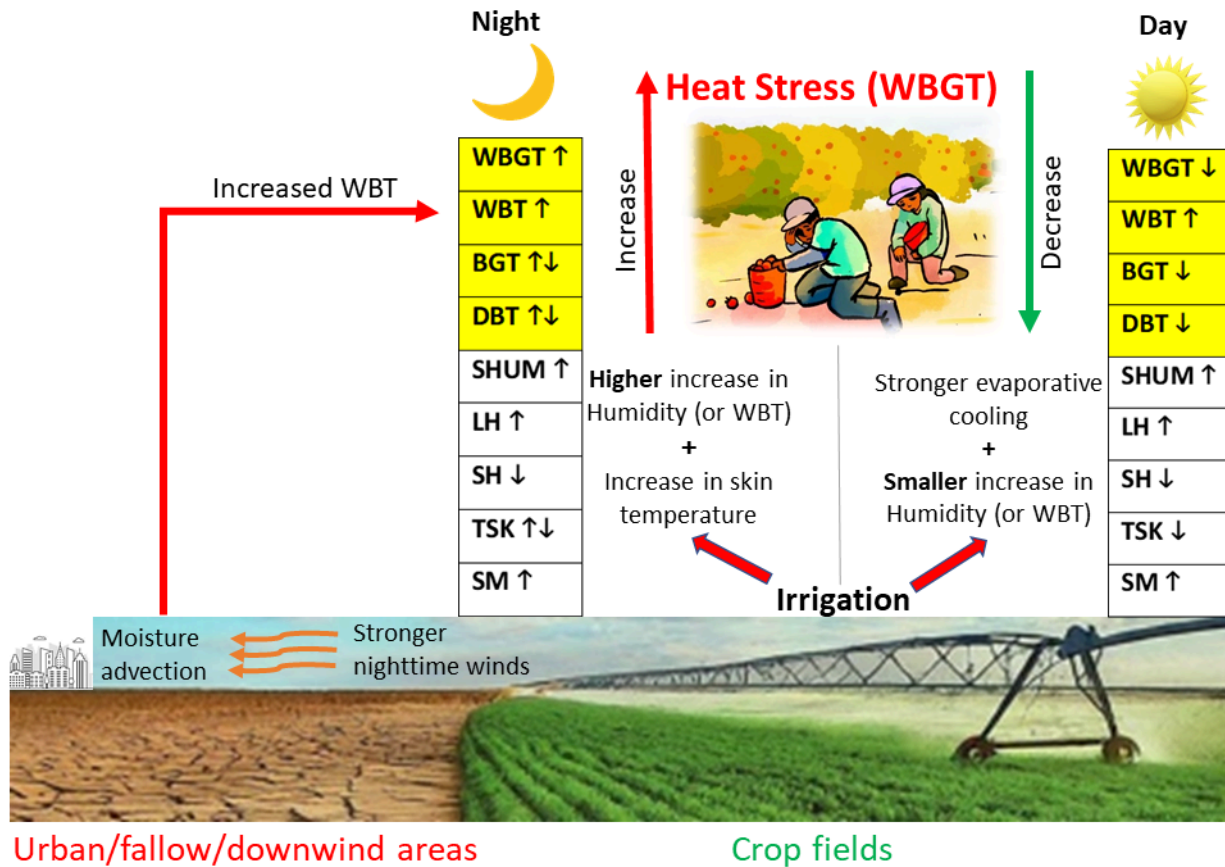


Fig. 9. Schematic diagram of the physical mechanisms involved in increasing or decreasing WBGT by irrigation in urban/fallow areas and crop fields. Abbreviations are: WBGT (Wet Bulb Globe Temperature), WBT (Wet Bulb Temperature), BGT (Black Globe Temperature), Dry Bulb Temperature (DBT), SHUM (Specific Humidity), LH (Latent Heat), SH (Sensible Heat), LST (Land Surface Temperature), SM (Soil Moisture). The parameters are listed in approximate order in which they get affected by irrigation beginning with SM. The upward and downward arrows represent the increasing and decreasing effect of irrigation, respectively.

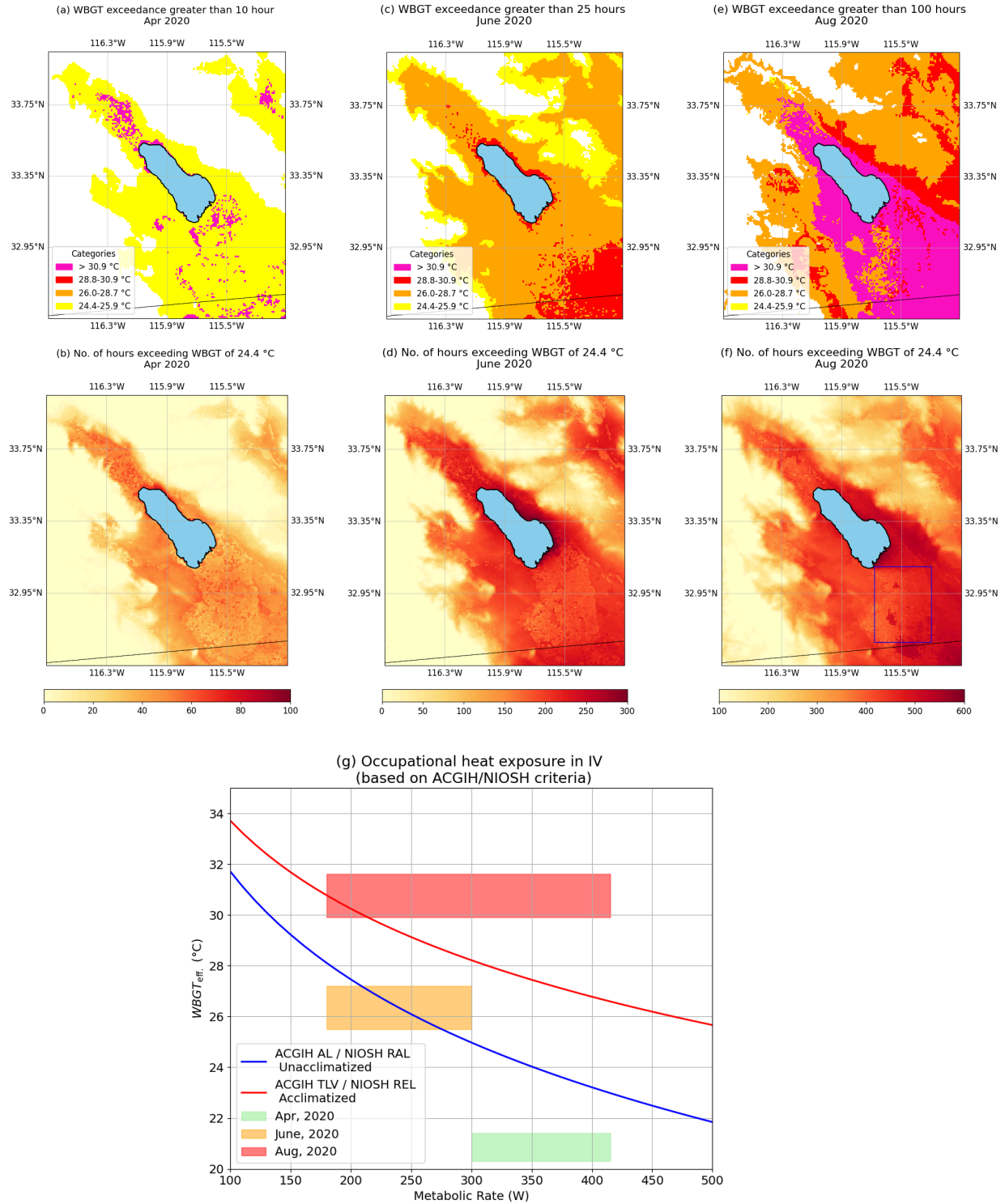


Fig. 10. WBGT exceedance hours during the harvest months of the year 2020. (a, c, e) as per WBGT limits for four different categories for Region 2^{66,88} representing extreme (pink), high (red), moderate (orange) and elevated (yellow) threat of heat stress, (b, d, f) total exceedance hours (WBGT > 24.4 °C) for April, June, and August, respectively. (g) Occupational heat stress exceedance for different months based on ACGIH⁸⁹/NIOSH⁹⁰ threshold limits.

WBGT exceedance map and distribution

The different components of WBGT (eq. 1) have different impacts on the final WBGT result (Supplementary Fig. S10). Considering average daily maximum values in April 2020 as reference, WBT, which has the largest weight in the WBGT equation, ranges from -5.8 to 30.0 °C while the BGT, which has the second largest weight, ranges from -2.2 to 64.4 °C. DBT, which has the smallest weight in the WBGT equation, has average daily maximum values in the range of -5.1 to 42.7 °C in April, 7.7 to 46.8 °C in June, and 15.3 to 49.9 °C in August (Fig. S10e). The resulting average daily maximum WBGT values, which are determined by the dynamic combination of the three components, range from -5.1 to 32.2 °C for April, 3.8 to 33.4 °C for June, and 8.8 to 37.1 °C for August, 2020.

Grundstein et al. (2015)⁶⁶ classified the conterminous US into three zones using WBGT climatology, recognizing that the heat stress thresholds are different in different climate regimes due to geographical variation in heat exposure and acclimatization. The IV lies in moderate climate zone (Region 2) where the WBGT thresholds are lower than the colder zone (Region 1) but higher than the warmer zone (Region 3). The WBGT exceedance map created using thresholds of WBGT for different heat stress categories in Region 2^{66,88} (Supplementary Table S3, S4) for the harvest months considered is presented in Figure 10. In April, WBGT in most of the crop fields in IV and Coachella Valley exceeds the 24.4-25.9 °C category while the Coachella valley and the southeastern region of the Salton Sea exceed the highest category (WBGT > 30.9 °C) (Fig. 10a), mainly due to the sharp rise in temperature in the last week of the month (Fig. 2). In June, WBGT exceeds 28.8-30.9 °C category around the shores of the Salton Sea and southeastern part of the IV crop fields while the lower category (26.0-28.7 °C) is exceeded in most parts of the domain including the crop fields (Fig. 10b). Similarly, in August, WBGT exceeds the highest category (WBGT > 30.9 °C) in most of the IV crop fields and the Coachella valley (Fig. 10c). While the total monthly exceedance hours (WBGT > 24.4 °C) in the IV crop fields occur only for about 50 hours in April, it occurs for more than 150 and 300 hours in June and August, respectively (Fig. 10b, d, f).

Figure S11 shows the number of hours exceeding the suggested WBGT threshold for prevention action (24.4 °C) as above but separately for daytime and nighttime in August. The crop fields of IV experience exceedance of 24.4 °C WBGT for more than ~300 (100) hours in the daytime (nighttime) (Fig. S11a, b). WBGT exceeds 24.4 °C for more than ~200 hours at nighttime on the southeastern side of the Salton Sea and in the cities of Mexicali, Westmoreland, and El Centro. This exceedance at night in August is noteworthy compared to April and June, which observed no such exceedance (not shown). These results are critically important because working in the nighttime could become more common in the future to avoid the daytime heat⁹¹. Many farm workers and their families live in cities where we observed the highest exceedance hours in the night. These families may lack air conditioning⁹², exposing them to heat during sleeping hours and potentially preventing the recovery from daytime heat exposure, which is a key contributor to heat stress symptoms.

We calculated the suggested occupational heat stress exceedance using the range of average daily maximum WBGT ($WBGT_{eff}$) within the crop fields (supplementary Fig. S6a, blue box) using reference metabolic rates¹⁵ and normal work clothing. The $WBGT_{eff}$ values exceed the thresholds even for the acclimatized workers given by American Conference of Governmental and Industrial Hygienists (ACGIH[®]) Threshold Limit Value (TLV)⁸⁹, also called the Recommended Exposure Limit (REL)⁹⁰ by the National Institute for Occupational Safety and Health (NIOSH), even for light work category (metabolic rate > 180 W). In June, heat stress exceeds for unacclimatized workers given by ACGIH[®] Action Limits (AL), also called Recommended Action Limit (RAL) by NIOSH, even for medium level of physical activity (metabolic rate > 275 W). In April, neither of these thresholds are exceeded.

Discussion and summary

We presented a robust high-resolution regional climate model (WRF) for irrigated agriculture and urban areas, with a case study in the Imperial Valley. We used the high-resolution output fields of WRF to calculate heat stress (Wet Bulb Globe Temperature) using the *thermofeel* python library⁷³. Although there are a few localized studies conducted in the Central Valley and Imperial Valley to assess heat stress^{11,48}, this study is the first that deploys a regional climate model to calculate WBGT at a crop field scale in the entire Imperial Valley. We also examined the impact of irrigation on heat stress in detail, in urban and cropped areas, and in daytime and nighttime. The spatial resolution of our WBGT simulation (1 km) closely represents the microclimate variability of the crop fields, whose typical size is $\sim 0.8 \text{ km} \times 0.8 \text{ km}$, and are often cultivated together to form a much larger effective crop field. We employed two-stage validation in this study, one for the input parameters including the black globe temperature, and another for the calculated WBGT, which ensures the robustness of our WBGT maps.

Irrigation impact on heat stress

Our results show that irrigation generally reduces WBGT during the daytime due to widespread evaporative cooling of the crop fields with average reduction in WBGT by 0.3-1.3 °C in summer. At night, irrigation increases WBGT by 0.4-1.3 °C, because the increase in WBT by the increased humidity becomes larger than the reduction in DBT and BGT by evaporative cooling. Increase in nighttime heat stress following irrigation is more prominent in the downwind areas as well as in the bordering areas of the crop fields where irrigation increases nighttime land surface temperature (Fig. S9). This warming is due to increased heat capacity and thermal conductivity of the soil, which increases energy storage during the daytime and contributes to the surface warming at night²². Irrigation also increases WBGT in nearby urban, fallow, and desert areas where the evaporative cooling is absent and the advected moisture from nearby crop fields increases the WBT. In summary, the key findings of this study are: 1) unlike WBT that is consistently amplified by irrigation (Fig. 7), WBGT can both increase and decrease in response to irrigation (Fig. 6), 2) the daytime WBGT generally decreases but nighttime WBGT is more likely to increase by irrigation, 3) whether WBGT is amplified or reduced may depend on the

background climate state, 4) irrigation also increases WBGT in urban, fallow, and desert areas nearby the irrigated crop fields.

Model error is reduced by including irrigation. The warm temperature bias is reduced in after including irrigation, which is consistent with previous studies^{25,93-96}. Our results of widespread cooling of crop fields due to irrigation are also consistent with previous studies^{19,20,23,24,27}. The increase in heat stress in the night is consistent with the results of Wouters et al. (2022)²³ and Mishra et al. (2020)²⁰ both of which showed increases in heat stress with increased humidity following irrigation²⁰ or during cooler periods²³. Our results also show an increase in WBGT at night (cooler period) due to a larger increase in humidity or WBT at night than in the daytime (Fig. 8). Our results provide more details on the irrigation effect on heat stress by showing that in the daytime the stronger evaporative cooling completely offsets the increase in WBT, resulting in reduced heat stress in crop fields. The negative (positive) effect of irrigation on WBGT in daytime (nighttime) is consistent with the results of a recent study⁹⁷ which showed decrease (increase) of heat stress in the daytime (nighttime) under cropland expansion scenario in global climate models.

Although the application of irrigation greatly improved the accuracy of modeled air temperature and humidity in the agricultural areas, improvement in urban areas was small. The model could potentially be improved further by more detailed scheduling of irrigation, and/or meter-scale simulation of urban areas⁹⁸, which is computationally intensive. The irrigation module applies water to bring the current soil moisture level to the field capacity, so the amount of water applied may not accurately represent the actual irrigation scenarios in the field, which differs by crop types, soil moisture conditions, and prevailing irrigation practices. Application of a fixed rate of irrigation at 0.30 mm hr^{-1} based on potential evapotranspiration for the region gave equivalent results; application of a high irrigation rate (2 mm hr^{-1}) eliminated the bias in the later half of the month but overestimated the humidity during the first half of the month (results not shown). This highlights the need to collect detailed field irrigation data that represent the diurnal, seasonal and spatial variation of irrigation in the crop fields, which are often not readily available, and to utilize them in irrigation modules for improving climate model simulations.

WBGT exceedance and policy relevance

Several previous studies have used either simplified WBGT^{58,99-102} or simply WBT¹⁰³⁻¹⁰⁵, both of which only include temperature and humidity to calculate heat stress under present and future climate because global climate model projections typically do not have radiation parameters. Many of the models used in these projections have biases in their output fields such as temperature and humidity^{25,29}, partly due to their coarse spatial resolution and partly because they do not include irrigation effects. We derive WBGT exceedances using a physics-based WBGT model *thermofeel* developed by Brimicombe et al. (2022)⁷³ that includes radiation and wind, using outputs from WRF with irrigation at 1-km spatial resolution, with validation. Brimicombe et al. (2022) method has shown similar geographic variability of WBGT compared to that obtained using the gold-standard method given by Liljegren et al. (2008), even during heatwaves⁷⁶. However, Brimicombe's method may give a biased estimate of WBGT in different

environments partly due to the use of empirically derived WBT in place of ‘natural’ WBT⁷⁵. Our results show no systematic over or underestimation of WBGT parameters in our study domain (Fig. 3). The empirical formulation of WBT given by Stull (2011)¹⁰⁶ employed in *thermofeel* has been widely used to quantify heat stress under present and future climate¹⁰²⁻¹⁰⁵. However, since the ‘natural’ WBT refers to the WBT measured under sun and wind, which is not the same as the approximated WBT¹⁰⁶ used by *thermofeel*, our results of WBGT exceedance might be conservative, particularly with respect to other WBGT formulations^{74,75}. Future studies should compare the simplified WBT given by Stull (2011)¹⁰⁶ and the natural WBT calculated by Liljegren et al. (2008)⁷⁴ method with instrument-measured natural WBT to quantify the biases and determine whether the WBGT exceedances differ significantly using the two approaches.

Our results highlight the need for more specified HRI (Heat-related Illness) prevention regulations across varied working hours and irrigation scenarios. Regulations and preventative actions to lower the risk of farmworker HRI should be evaluated for workers in nighttime hours in irrigated crop environments. The exceedances of NWS WBGT thresholds for HRI preventative actions, particularly during nighttime hours, also suggest that regulatory adherence should be monitored for workers both in the workspace as well as in their dwelling space (often urban areas). A recent study using recorded and simulated weather data based on HRIs reported to OSHA shows that almost every incidence of HRI occurred when heat stress exceeded ACGIH^{®89}/NIOSH⁹⁰ WBGT occupational exposure limits, with 88% sensitivity for incidence of HRI in acclimated workers and 97% for non-acclimated workers, while the sensitivity was at least 92% and up to 100% for HRI fatalities¹⁰⁷.

Although WBGT is a more reliable measure of heat stress than air temperature in outdoor environments and is considered the current standard for assessing heat stress^{37,90}, current regulations in California rely on individual workers and farm managers to monitor heat exceedance using air temperature forecasts alone⁴³. Heat stress begins to occur at a much lower WBGT threshold in the IV region (24.4 °C) than the generally perceived high air temperature (95 °F or 35 °C) used in T8 §3395 CCR⁴³. This WBGT threshold is frequently exceeded in the summer months (Fig. 10), suggesting that Cal/OSHA should consider adopting WBGT based thresholds in formulating heat related policies for farmworkers.

The above policy shortcoming may be related to the cost and other restrictive barriers of direct measurement of WBGT in agricultural contexts, which can be complemented by leveraging regional climate modeling for heat stress modeling and prevention of HRI in those settings. Simple heat indices have been used previously to quantify heat stress more often than WBGT because measured WBGT data are not commonly available^{52,67}. Forecasting WBGT using a high-resolution regional weather/climate model thus offers the opportunity for developing more specified HRI preventative action plans for farm managers and owners to better communicate dangerous heat conditions. In the recent context of increasing heat waves globally³ and in California¹, our research can also help develop climate change adaptation strategies at the local level.

Methods

Observational data and validation

We use three meteorological data sources for validation: California Irrigation Management Information System (CIMIS), California Air Resources Board (CARB) and stations installed by us for three locations starting in May 2024: Westmorland, El Centro, and Coachella. Our stations included the BGT sensors at 1.1-m height from the ground except for El Centro, which was on the roof of a building. The CIMIS was developed by the California Department of Water Resources together with the University of California, Davis in 1982 that manages a network of over 145 automated weather stations in California. We use the meteorological data from CARB's Air quality management information system (AQMS2), which collects data from various sources and applies basic quality control measures. The location of stations used in this study is presented in Figure 1b with CIMIS in green, CARB in red, and our stations in white. The temperature and humidity fields at both CARB and CIMIS sites are typically measured at 1.8-2m height from the ground of the installation surface, which are compared with model simulated fields at 2-m height. Winds are typically measured at 10-m height for CARB and 2-m for CIMIS sites. For this reason, model winds, which correspond to 10-m height, are compared only at CARB sites.

We validate model-derived WBGT against station-derived values as commonly done in the literature⁷⁶. When measurements of black globe temperature (BGT) are not available for the model period, we conduct validation using two terms (first and third) of eq (1) which together constitute 80% weight of WBGT, excluding BGT, which is only 20%.

All results correspond to the final model with irrigation, all validations are performed for April 2020, and all heat stress calculations are performed for the harvesting months of April, June, and August, 2020. The BGT measurements were made recently in the IV fields so the validation of BGT is performed separately for a more recent period (May 21-June 22, 2024).

WRF-modeling

We use WRF version 4.4 in this study. Our WRF model configuration consists of three nested domains with spatial resolution of 9, 3, and 1 km for d01, d02, and d03, respectively (Fig. 1a). The innermost domain d03 covers the entire cultivated lands of the Imperial Valley and part of Coachella Valley in the north. Because more than half of the farm workers working in the IV area commute daily across the border from the Mexicali City, we also include Mexicali and its surroundings to better account for the farmworkers' heat exposure.

We use ERA5 data developed by European Centre for Medium-Range Weather Forecasts (ECMWF) as initial and boundary conditions, which replaces the widely used ERA-interim data, and provides hourly estimates although at a coarse (31 km) resolution (Hersbach et al., 2020). We explicitly resolve convection in our innermost domain (d03) which is configured at 1 km spatial resolution and we use parameterized convection in the two parent domains (d01, d02) using Grell and Freitas scheme¹⁰⁸ (cu_physics = 3), which is a scale and aerosol-aware scheme. We use Morrison double-moment microphysics scheme¹⁰⁹, Yonsei University Scheme (YSU)

planetary boundary layer scheme¹¹⁰, Rapid Radiative Transfer Model (RRTMG) for both shortwave and longwave radiation¹¹¹, and revised MM5 Monin-Obukhov surface layer scheme¹¹². We apply grid nudging for u and v components of wind speed, temperature, and water vapor mixing ratio at 6-hourly intervals with strengths 0.0006, 0.0003, and 0.00003, respectively but only above the PBL, which is a more common practice.

Land surface model

We use the state-of-the-art community Noah-MP land surface model¹¹³ within WRF, which has been successfully used to produce high-resolution hydroclimate over the continental US¹¹⁴. Noah MP allows different treatment of LAI, from input data, from lookup table and even its dynamic prediction, if dynamic vegetation option is used. We use a generic dynamic vegetation model (dveg=7) that calculates energy and water flux exchange in vegetated areas using the prescribed vegetation information from the input data of LAI and FPAR (GREENFRAC). Note that this option doesn't include a crop model and nitrogen and phosphorus cycles are currently not included in Noah MP.

LAI (m^2/m^2) is the ratio of one-sided leaf area to ground cover area, which is the projected area of canopy leaves when looked from above. LAI is used in the model for several calculations including calculation of latent heat conductance due to plant transpiration, photosynthesis rate, maximum liquid water held by canopy and some carbon processes¹¹³. FPAR is the fraction of photosynthetically active radiation (400-700 nm) absorbed by green vegetation. FPAR/GREENFRAC is used to calculate a number of parameters related to energy balance including calculation of interception and throughfall, heat exchange through canopy, net surface longwave emissivity, and in the calculation of 2-m air temperature over vegetated areas¹¹³.

Accurate representation of LAI and FPAR is key in simulating the land-atmosphere interactions of energy, momentum, and water fluxes realistically. The original implementation of WRF uses the LAI/FPAR data derived from this original MODIS data using climatological average data between 2001-2010, similar to the MODIS-derived land cover climatology¹¹⁵, which we use in this study as the land use data (modis_landuse_20class_30s_with_lakes) available at 30 arc-sec spatial resolution. This land use data has 21 land use categories in which 12 (croplands) and 14 (cropland/natural vegetation mosaic) categories correspond to the croplands. For albedo, we use climatological data derived from MODIS instead of table values, which is available at 0.05 degree resolution.

The original MODIS LAI/FPAR data were developed jointly by Boston University, University of Montana and NASA GSFC, using an algorithm that used spectral information content of MODIS surface reflectance at up to 7 spectral bands (red and near-infrared) over leaf canopies in a radiative transfer equation, and a complimentary backup algorithm that used NDVI to calculate LAI in pixels where certain conditions are not met¹¹⁶. WRF, by default, uses a 10 arc-min resolution version of this MODIS LAI and 30 arc-sec version of FPAR (GREENFRAC) data. However, it is possible to use the 30 arc-sec (~ 0.9 km) version of the LAI data by modifying the geogrid table.

The default MODIS data for WRF uses climatological average, which does not represent the actual land cover profile in a particular year, which is problematic in agricultural areas where crop type and land cover can change annually. To better represent the LAI/FPAR distribution over the study area and change over time, we conducted our simulations using new sensor-independent LAI/FPAR data from Pu et al. (2023)¹¹⁷, which improved the original MODIS LAI/FPAR algorithm described in MODIS algorithm theoretical basis document¹¹⁶. They consolidated the original MODIS (Aqua and Terra) and VIIRS LAI/FPAR product and applied rigorous quality control criteria and a spatial-temporal tensor extrapolation model for gap filling, which shows significant improvement over the original data. This new LAI data also has a higher spatial resolution (~0.5 km) compared to 30 arc-sec (~0.9 km) for the existing climatological data.

We apply irrigation within Noah-MP based on LAI threshold using the USDA county level irrigation data¹¹⁸. In our current Noah-MP model configuration, first the croplands are identified from MODIS land use data (`modis_landuse_20class_30s_with_lakes`) corresponding to the land use category of 12 (croplands) and 14 (cropland/natural vegetation mosaic). Then the irrigation fraction data (IRFRACT) from USDA county level irrigation data is used to determine where to irrigate, i.e., grid cells with $IRFRACT > 0.1$, which has been reduced to 0.05 in this study. The irrigation is triggered in the model using a minimum LAI value of 0.1^{113,118}, which has also been reduced to 0.05 to avoid omission of any irrigated lands. The irrigation is applied using the sprinkler irrigation option until the soil moisture reaches the field capacity, which is the default setting. We also conducted additional sensitivity tests to apply sprinkler irrigation continuously at different rates (0.30 and 2 $mm\ hr^{-1}$) by modifying the source code.

WBG T calculations

We use *thermofeel* python library⁷³ developed and maintained by ECMWF for the WBG T calculations. *thermofeel* is a set of python libraries used to calculate various thermal indices including WBG T using standard meteorological outputs.

In the absence of measured natural wet bulb temperature, the WBT is approximated using an empirical equation given by Stull (2011)¹⁰⁶ as a function of relative humidity and air temperature⁷³:

$$WBT = t2_c \times \arctan [0.151977 \times \sqrt{(rh + 8.313659)} + \arctan (t2_c + rh) - \arctan (rh - 1.676331) + 0.00391838 \times (rh)^{3/2} \times \arctan (0.023101 \times rh) - 4.686035 \quad (2)$$

where, rh is relative humidity and $t2_c$ is air temperature in Celsius.

In the absence of measured globe temperature (GT), *thermofeel* calculates GT from mean radiant temperature (MRT), which can be calculated using commonly available gridded parameters from model/reanalysis such as ERA5⁷⁶. The MRT, which was introduced to parameterize the effects of the complex radiant environment in one temperature-dimension index, is defined as the uniform temperature of a hypothetical black sphere that exchanges the same amount of radiation with a human body as the actual surroundings¹¹⁹. *thermofeel* calculates MRT using equation (14) in Di

Napoli et al. 2020¹²⁰, which calculates MRT as a function of solar and thermal radiation including the direct solar radiation, diffuse solar radiation, and thermal radiation (longwave), all of which are crucial to characterize heat exposure on a human body and are commonly available in most climate model outputs and reanalysis data.

The first step in computing MRT is to calculate surface projection factor f_p , which represents the portion of the human body exposed to direct solar radiation. The f_p is given by an empirical equation derived in terms of solar elevation angle as below¹²¹:

$$f_p = 0.308 \cos(\gamma (0.998 - \gamma^2/50000)) \quad (3)$$

where γ is the solar elevation angle as defined in Table 2.

As per the definition of MRT, the MRT can be obtained by equating the radiant heat absorbed by a human body to the radiation emitted by a fictive black-body emitter that emits radiant energy equal to σT_{mrt}^4 , solving which we get¹²²

$$T_{mrt} = \left\{ \frac{1}{\sigma} \left[f_a strd + f_a lur + \frac{\alpha_{ir}}{\epsilon_p} (f_a dsw + f_a rsw + f_p dsrp) \right] \right\}^{1/4} \quad (4)$$

The input parameters in the above equations and their equivalent in WRF are defined in Table 2.

σ is the Stefan-Boltzmann constant $5.67 \times 10^{-8} \text{ Wm}^{-2} \text{ K}^{-4}$, f_a is the angle factor set to 0.5

assuming a standing human being receiving radiation from ground and sky only (is much more complex in an urban setting), α_{ir} is the effective shortwave absorption coefficient of the human body assumed to be 0.7 and ϵ_p is the effective emissivity of the clothed human body assumed to be 0.97.

thermofeel approximates the direct solar radiation (at surface) on a plane perpendicular to the direction of the Sun (dsrp) based on total sky direct solar radiation (fdir) and cosine of zenith angle (cossza). However, in our case, WRF provides dsrp, so we are not approximating as such. The WRF equivalent variable of dsrp is SWDDNI (Table 2). The SWDDNI and other radiation fields (Table 2) necessary for calculating BGT, which are not standard outputs, can be added to the output stream by adding the following line in the file myoutfields.txt in the WRF directory: +:h:0:SWDDIR,SWDDIF,SWDDNI. The Google Colab scripts provided in the data availability section shows how to use different meteorological and radiation outputs from WRF to calculate WBGT.

Table 2. Input parameters for calculating WBGT and their WRF equivalent output variables.

Parameters	<i>thermofeel</i> variable	Equivalent WRF output variable name	Remarks
Dew point temperature at 2m	td_k (K)	Td_2m (K)	Calculated with the NCAR NCL script wrfout to cf
Air temperature at 2m	t2_k (K)	T2 (K)	Standard wrf output
Relative humidity at 2m	rh (%)	rh_2m (%)	Calculated with the NCAR NCL script wrfout to cf
Wind speed at 10m height	va ($m s^{-1}$)	WS ($m s^{-1}$) = $\sqrt{(U10^2 + V10^2)}$	Calculated from standard WRF output U10 and V10
Cosine of solar zenith angle	cossza ($^{\circ}$)	COSZEN cos of solar zenith angle	Standard wrf output
Solar elevation angle	γ ($^{\circ}$) = 90-cossza	-	-
Total sky direct solar radiation at surface (downward on a horizontal plane)	fdir ($W m^{-2}$)	SWDDIR Shortwave surface downward direct irradiance ($W m^{-2}$)	Not a standard WRF output, added in myoutfields.txt
Surface solar radiation downwards	ssrd ($W m^{-2}$)	SWDOWN ($W m^{-2}$) downward short-wave flux at ground surface	Standard wrf output
Surface thermal radiation downwards	strd ($W m^{-2}$)	GLW ($W m^{-2}$) downward long wave flux at ground surface	Standard wrf output
Surface solar radiation upwards	rsw = ssrd-ssr	SWUPB ($W m^{-2}$) instantaneous upwelling shortwave flux at bottom	Standard wrf output
Surface thermal radiation upwards	lur = strd-strr	LWUPB ($W m^{-2}$) instantaneous upwelling longwave flux at bottom	Standard wrf output
Surface net solar radiation	ssr ($W m^{-2}$)	SWDOWN-SWUPB	Required for calculating mean radiant temperature
Surface net thermal radiation	strr ($W m^{-2}$)	GLW-LWUPB	Required for calculating mean radiant temperature
Direct solar radiation (at surface) on a plane perpendicular to the direction of the Sun	dsrp ($W m^{-2}$)	SWDDNI Shortwave surface downward direct normal irradiance ($W m^{-2}$)	Not a standard WRF output, added in myoutfields.txt
Diffuse solar radiation	dsw = ssrd-fdir	SWDDIF Shortwave surface downward diffuse irradiance ($W m^{-2}$)	Not a standard WRF output, added in myoutfields.txt

The black globe temperature (BGT) is then calculated as a function of MRT calculated above using the equation provided by Guo et al. 2018 (eqn 6), which was originally developed by de Dear (1988) using the heat balance equation on a ping-pong globe thermometer^{123,124}. The globe temperature is calculated by rearranging the equation (5) below as in Thorsson et al. (2007)¹²⁵.

$$T_{mrt} = \sqrt[4]{T_g^4 + \frac{1.1 \times 10^8 \times v_a^{0.6}}{\epsilon D^{0.4}} (T_g - T_a)} \quad (5)$$

where, 1.1×10^8 is an empirical derived parameter, v_a is the wind speed at the globe level (1.1 m) in ms^{-1} , which is calculated by logarithmically downscaling the modeled 10-m wind speed to 1.1 m, and ϵ is the emissivity of the globe equal to 0.95. D is the diameter of the globe (0.15 m).

Statistics

For comparing model results with observations, model grid cells closest to the station coordinate are extracted using the great circle method. Pearson's correlation coefficient (Rho) is used to assess correlations and root mean squared error (RMSE) is used to characterize the errors between model and observations.

A two-sided difference of mean t-test is applied to find the grid cells with statistically significant difference between irrigation and no-irrigation WRF simulations using hourly model output data. The t-statistics used is given by,

$$t = \frac{\bar{X}_1 - \bar{X}_2}{Sp \sqrt{\frac{2}{n}}} \quad (6)$$

Where, \bar{X}_1 and \bar{X}_2 are the sample means, Sp is the pooled standard deviation given by,

$$Sp = \sqrt{\frac{s_{x_1}^2 + s_{x_2}^2}{2}} \quad (7)$$

and n is the number of samples,

The t-test is performed at each grid cell of the model (d03), the size of which is 171 (lat) \times 162 (lon). The p-values are also calculated and reported for each grid cell. The number of samples at each grid cell is 720 (24 \times 31) for April and June, and 744 (24 \times 31) for August. Half sets of this hourly data between 7 AM-6 PM and 7 PM-6 AM were used for the daytime and nighttime calculations, respectively.

Data availability

ERA5 data were downloaded from the following NCAR repository:

<https://rda.ucar.edu/datasets/ds633-0/>. WRF static data were downloaded from the following UCAR page: https://www2.mmm.ucar.edu/wrf/users/download/get_sources_wps_geog.html

The sensor-independent LAI/FPAR data were obtained from Google Earth Engine; the details of which is made available by the data developers at

https://github.com/JiabinPu/Sensor-Independent-LAI-FPAR-CDR/blob/master/GEEExample_Re

ad_SI_LAI_FPAR_CDR_8d.txt. CIMIS data was downloaded from:
<https://cimis.water.ca.gov/WSNReportCriteria.aspx>. CARB data were obtained from:
<https://www.arb.ca.gov/aqmis2/metsselect.php>.

Code Availability

WRF source code can be obtained from the Github repository:
<https://github.com/wrf-model/WRF>. *thermofeel* v2.0.0 python package is available from
<https://pypi.org/project/thermofeel/>. Python scripts used to perform data analysis, and produce figures, are made available at the Github repository:
<https://github.com/psagar123/RuralHeatIsland>.

Acknowledgements

The first author is grateful to Rodrigo Moreira and Jiabin Pu for their assistance in obtaining the LAI/FPAR data from Google Earth Engine. We acknowledge the entire Rural Heat Island team for contributing to the discussions on this work. This research is funded by the University of California Office of the President (UCOP) Climate Action Grant award R02CP7521 “Rural heat islands: Mapping and mitigating farmworker exposure to heat stress”. Computational work of this research was carried out at Expanse supercomputer at San Diego Supercomputing Center through the ACCESS program of the National Science Foundation. We are grateful to the two anonymous reviewers whose comments significantly enhanced the value and readability of this manuscript.

Author Contributions

S.P.P. carried out model experiments, performed data analysis, and wrote the manuscript. T.B. conceived the project idea, supervised the overall project, and edited the manuscript. F.S. and M.A.Z.P. helped design the WRF model experiments and edited the manuscript. C.H. provided guidance in carrying out irrigation simulations using Noah-MP. C.J. and C.T. took part in the discussions and edited the manuscript. N.L.G. conceived the idea of using WBGT for farmers’ heat stress. H.C. contributed to writing sections on literature related to public health. T.Q. and C.N. provided support for *thermofeel* library and edited the manuscript. A.M., T.H.Y., and M.S. helped with instrument setup and data collection from the BGT sensors.

Competing Interests

The authors declare no competing interests.

Reference list

- 1 Ostro, B. D., Roth, L. A., Green, R. S. & Basu, R. Estimating the mortality effect of the July 2006 California heat wave. *Environmental Research* 109, 614-619 (2009).
- 2 Russo, S. et al. Magnitude of extreme heat waves in present climate and their projection in a warming world. *Journal of Geophysical Research: Atmospheres* 119, 5105-5112 (2014).
- 3 Rousi, E., Kornhuber, K., Beobide-Arsuaga, G., Luo, F. & Coumou, D. Accelerated western European heatwave trends linked to more-persistent double jets over Eurasia. *Nature communications* 13, 3851 (2022).
- 4 Domeisen, D. I. et al. Prediction and projection of heatwaves. *Nature Reviews Earth & Environment* 4, 36-50 (2023).
- 5 Jackson, L. L. & Rosenberg, H. R. Preventing heat-related illness among agricultural workers. *Journal of agromedicine* 15, 200-215 (2010).
- 6 Fatima, S. H., Rothmore, P., Giles, L. C., Varghese, B. M. & Bi, P. Extreme heat and occupational injuries in different climate zones: A systematic review and meta-analysis of epidemiological evidence. *Environment international* 148, 106384 (2021).
- 7 NIOSH. Heat Stress first aid for heat illnesses. 2024-100 (2023).
<<https://doi.org/10.26616/NIOSH PUB2024100>>.
- 8 Moyce, S. et al. Heat strain, volume depletion and kidney function in California agricultural workers. *Occupational and environmental medicine* 74, 402-409 (2017).
- 9 Smith, D. J. et al. Heat stress and kidney function in farmworkers in the US: a scoping review. *Journal of Agromedicine* 27, 183-192 (2022).
- 10 Vega-Arroyo, A. J. et al. Impacts of weather, work rate, hydration, and clothing in heat-related illness in California farmworkers. *American journal of industrial medicine* 62, 1038-1046 (2019).
- 11 Langer, C. E. et al. Are Cal/OSHA regulations protecting farmworkers in California from heat-related illness? *Journal of occupational and environmental medicine* 63, 532-539 (2021).
- 12 Stoecklin-Marois, M., Hennessy-Burt, T., Mitchell, D. & Schenker, M. Heat-related illness knowledge and practices among California hired farm workers in the MICASA study. *Industrial health* 51, 47-55 (2013).
- 13 Dillane, D. & Balanay, J. A. G. Comparison between OSHA-NIOSH Heat Safety Tool app and WBGT monitor to assess heat stress risk in agriculture. *Journal of occupational and environmental hygiene* 17, 181-192 (2020).
- 14 Tigchelaar, M., Battisti, D. S. & Spector, J. T. Work adaptations insufficient to address growing heat risk for US agricultural workers. *Environmental research letters: ERL [Web site]* 15, 094035 (2020).
- 15 Wagoner, R. S. et al. An occupational heat stress and hydration assessment of agricultural workers in North Mexico. *International journal of environmental research and public health* 17, 2102 (2020).
- 16 Zhou, X. & Chen, H. Impact of urbanization-related land use land cover changes and urban morphology changes on the urban heat island phenomenon. *Science of the Total Environment* 635, 1467-1476 (2018).
- 17 Li, Y., Schubert, S., Kropp, J. P. & Rybski, D. On the influence of density and morphology on the Urban Heat Island intensity. *Nature communications* 11, 2647 (2020).
- 18 Qian, Y. et al. Urbanization impact on regional climate and extreme weather: Current understanding, uncertainties, and future research directions. *Advances in Atmospheric Sciences* 39, 819-860 (2022).
- 19 Yang, Q., Huang, X. & Tang, Q. Irrigation cooling effect on land surface temperature across China based on satellite observations. *Science of the total environment* 705, 135984 (2020).

- 20 Mishra, V. et al. Moist heat stress extremes in India enhanced by irrigation. *Nature Geoscience* 13, 722-728 (2020).
- 21 Payero, J. O., Tarkalson, D. D., Irmak, S., Davison, D. & Petersen, J. L. Effect of irrigation amounts applied with subsurface drip irrigation on corn evapotranspiration, yield, water use efficiency, and dry matter production in a semiarid climate. *Agricultural water management* 95, 895-908 (2008).
- 22 Chen, X. & Jeong, S.-J. Irrigation enhances local warming with greater nocturnal warming effects than daytime cooling effects. *Environmental research letters* 13, 024005 (2018).
- 23 Wouters, H. et al. Soil drought can mitigate deadly heat stress thanks to a reduction of air humidity. *Science advances* 8, eabe6653 (2022).
- 24 Lobell, D. B., Bonfils, C. & Faurès, J.-M. The Role of Irrigation Expansion in Past and Future Temperature Trends. *Earth Interactions* 12, 1-11 (2008). <https://doi.org/10.1175/2007E1241.1>
- 25 Lobell, D. et al. Regional Differences in the Influence of Irrigation on Climate. *Journal of Climate* 22, 2248-2255 (2009). <https://doi.org/10.1175/2008JCLI2703.1>
- 26 Lobell, D. B., Bonfils, C. J., Kueppers, L. M. & Snyder, M. A. Irrigation cooling effect on temperature and heat index extremes. *Geophysical Research Letters* 35 (2008). <https://doi.org/10.1029/2008GL034145>
- 27 Jha, R., Mondal, A., Devanand, A., Roxy, M. & Ghosh, S. Limited influence of irrigation on pre-monsoon heat stress in the Indo-Gangetic Plain. *Nature Communications* 13, 4275 (2022).
- 28 Andrade, C. W. et al. Climate change impact assessment on water resources under RCP scenarios: A case study in Mundaú River Basin, Northeastern Brazil. *International Journal of Climatology* 41, E1045-E1061 (2021).
- 29 Jones, C., Carvalho, L. M., Duine, G.-J. & Zigner, K. Climatology of Sundowner winds in coastal Santa Barbara, California, based on 30 yr high resolution WRF downscaling. *Atmospheric Research* 249, 105305 (2021).
- 30 Kong, Q. & Huber, M. Regimes of Soil Moisture–Wet-Bulb Temperature Coupling with Relevance to Moist Heat Stress. *Journal of Climate* 36, 7925-7942 (2023). <https://doi.org/10.1175/JCLI-D-23-0132.1>
- 31 Huang, X. & Ullrich, P. A. Irrigation impacts on California's climate with the variable-resolution CESM. *Journal of Advances in Modeling Earth Systems* 8, 1151-1163 (2016). <https://doi.org/10.1002/2016MS000656>
- 32 Krakauer, N. Y., Cook, B. I. & Puma, M. J. Effect of irrigation on humid heat extremes. *Environmental Research Letters* 15, 094010 (2020).
- 33 Steadman, R. G. The assessment of sultriness. Part I: A temperature-humidity index based on human physiology and clothing science. *Journal of Applied Meteorology and Climatology* 18, 861-873 (1979).
- 34 Ioannou, L. G. et al. Indicators to assess physiological heat strain—Part 1: Systematic review. *Temperature* 9, 227-262 (2022).
- 35 Simpson, C. H., Brousse, O., Ebi, K. L. & Heaviside, C. Commonly used indices disagree about the effect of moisture on heat stress. *npj Climate and Atmospheric Science* 6, 78 (2023). <https://doi.org/10.1038/s41612-023-00408-0>
- 36 Cooper, E. et al. An evaluation of portable wet bulb globe temperature monitor accuracy. *Journal of athletic training* 52, 1161-1167 (2017).
- 37 Iso, B. 7243: Ergonomics of the thermal environment—assessment of heat stress using the wbgt (wet bulb globe temperature) index. *Int Org Standard Geneva Switzerland* (2017).
- 38 Minard, D. Prevention of heat casualties in Marine Corps recruits: period of 1955–60, with comparative incidence rates and climatic heat stresses in other training categories. *Military medicine* 126, 261-272 (1961).
- 39 Budd, G. M. Wet-bulb globe temperature (WBGT)—its history and its limitations. *Journal of science and medicine in sport* 11, 20-32 (2008).

- 40 HeatRisk. HeatRisk, <<https://www.wpc.ncep.noaa.gov/heatrisk/>> (2024).
- 41 CalHeatScore. California Communities Extreme Heat Scoring System, <<https://calheatscore.calepa.ca.gov/>> (2024).
- 42 Rivas, L. Extreme heat: statewide extreme heat ranking system. (2022). <https://leginfo.legislature.ca.gov/faces/billNavClient.xhtml?bill_id=202120220AB2238>.
- 43 CCR. Heat illness prevention in outdoor places of employment. 8 (2005). <<https://www.dir.ca.gov/Title8/3395.html>>.
- 44 Buzan, J. R. Implementation and Evaluation of Wet Bulb Globe Temperature Within Non-Urban Environments in the Community Land Model Version 5. *Journal of Advances in Modeling Earth Systems* 16, e2023MS003704 (2024). <https://doi.org/https://doi.org/10.1029/2023MS003704>
- 45 Parajuli, S. P. et al. Effect of dust on rainfall over the Red Sea coast based on WRF-Chem model simulations. *Atmospheric Chemistry and Physics* 22, 8659-8682 (2022).
- 46 Cobb, A. et al. West-WRF 34-Year Reforecast: Description and Validation. *Journal of Hydrometeorology* 24, 2125-2140 (2023).
- 47 Ohashi, Y., Kikegawa, Y., Ihara, T. & Sugiyama, N. Numerical simulations of outdoor heat stress index and heat disorder risk in the 23 wards of Tokyo. *Journal of Applied Meteorology and Climatology* 53, 583-597 (2014).
- 48 Mitchell, D. C. et al. Physical activity and common tasks of California farm workers: California Heat Illness Prevention Study (CHIPS). *Journal of occupational and environmental hygiene* 15, 857-869 (2018).
- 49 Mix, J. M. et al. Physical activity and work activities in Florida agricultural workers. *Am J Ind Med* 62, 1058-1067 (2019). <https://doi.org/10.1002/ajim.23035>
- 50 Langer, C. E. et al. How Does Environmental Temperature Affect Farmworkers' Work Rates in the California Heat Illness Prevention Study? *Journal of Occupational and Environmental Medicine* 65 (2023).
- 51 Mizelle, E., Larson, K. L., Bolin, L. P. & Kearney, G. D. Fluid Intake and Hydration Status Among North Carolina Farmworkers: A Mixed Methods Study. *Workplace Health & Safety* 70, 532-541 (2022). <https://doi.org/10.1177/21650799221117273>
- 52 Clark, J. & Konrad, C. E. Observations and Estimates of Wet-Bulb Globe Temperature in Varied Microclimates. *Journal of Applied Meteorology and Climatology* 63, 305-319 (2024). <https://doi.org/https://doi.org/10.1175/JAMC-D-23-0078.1>
- 53 Sheridan, S. C., Allen, M. J., Lee, C. C. & Kalkstein, L. S. Future heat vulnerability in California, Part II: projecting future heat-related mortality. *Climatic Change* 115, 311-326 (2012).
- 54 Schwingshackl, C., Sillmann, J., Vicedo-Cabrera, A. M., Sandstad, M. & Aunan, K. Heat stress indicators in CMIP6: estimating future trends and exceedances of impact-relevant thresholds. *Earth's Future* 9, e2020EF001885 (2021).
- 55 Vargas Zeppetello, L. R., Raftery, A. E. & Battisti, D. S. Probabilistic projections of increased heat stress driven by climate change. *Communications Earth & Environment* 3, 183 (2022).
- 56 Weatherly, J. W. & Rosenbaum, M. A. Future Projections of Heat and Fire-Risk Indices for the Contiguous United States. *Journal of Applied Meteorology and Climatology* 56, 863-876 (2017). <https://doi.org/https://doi.org/10.1175/JAMC-D-16-0068.1>
- 57 Hall, A., Horta, A., Khan, M. R. & Crabbe, R. A. Spatial analysis of outdoor wet bulb globe temperature under RCP4.5 and RCP8.5 scenarios for 2041–2080 across a range of temperate to hot climates. *Weather and Climate Extremes* 35, 100420 (2022). <https://doi.org/https://doi.org/10.1016/j.wace.2022.100420>
- 58 Williams, E., Funk, C., Peterson, P. & Tuholske, C. High resolution climate change observations and projections for the evaluation of heat-related extremes. *Scientific Data* 11, 261 (2024). <https://doi.org/10.1038/s41597-024-03074-w>

- 59 Hulley, G., Shivers, S., Wetherley, E. & Cudd, R. New ECOSTRESS and MODIS land surface temperature data reveal fine-scale heat vulnerability in cities: A case study for Los Angeles County, California. *Remote Sensing* 11, 2136 (2019).
- 60 Taha, H. Characterization of urban heat and exacerbation: Development of a heat island index for California. *Climate* 5, 59 (2017).
- 61 McRae, I. et al. Integration of the WUDAPT, WRF, and ENVI-met models to simulate extreme daytime temperature mitigation strategies in San Jose, California. *Building and Environment* 184, 107180 (2020).
- 62 Yaglou, C. & Minard, D. Control of heat casualties at military training centers. *Arch. Indust. Health* 16, 302-316 (1957).
- 63 Lemke, B. & Kjellstrom, T. Calculating workplace WBGT from meteorological data: a tool for climate change assessment. *Industrial health* 50, 267-278 (2012).
- 64 Brocherie, F. & Millet, G. P. Is the wet-bulb globe temperature (WBGT) index relevant for exercise in the heat? *Sports Medicine* 45, 1619-1621 (2015).
- 65 Spangler, K. R. et al. Does choice of outdoor heat metric affect heat-related epidemiologic analyses in the US Medicare population? *Environmental Epidemiology* 7, e261 (2023).
- 66 Grundstein, A., Williams, C., Phan, M. & Cooper, E. Regional heat safety thresholds for athletics in the contiguous United States. *Applied geography* 56, 55-60 (2015).
- 67 Bernard, T. E. & Barrow, C. A. Empirical approach to outdoor WBGT from meteorological data and performance of two different instrument designs. *Industrial health* 51, 79-85 (2013).
- 68 Bernard, T. E. & Iheanacho, I. Heat Index and Adjusted Temperature as Surrogates for Wet Bulb Globe Temperature to Screen for Occupational Heat Stress. *Journal of Occupational and Environmental Hygiene* 12, 323-333 (2015). <https://doi.org/10.1080/15459624.2014.989365>
- 69 Turco, S. N. et al. in *Livestock Environment VIII*, 31 August–4 September 2008, Iguassu Falls, Brazil. 122 (American Society of Agricultural and Biological Engineers).
- 70 Ashley, C. D., Luecke, C. L., Schwartz, S. S., Islam, M. Z. & Bernard, T. E. Heat strain at the critical WBGT and the effects of gender, clothing and metabolic rate. *International Journal of Industrial Ergonomics* 38, 640-644 (2008).
- 71 Racinais, S. et al. Consensus recommendations on training and competing in the heat. *Scandinavian journal of medicine & science in sports* 25, 6-19 (2015).
- 72 Wolf, S. T., Folkerts, M. A., Cottle, R. M., Daanen, H. A. & Kenney, W. L. Metabolism-and sex-dependent critical WBGT limits at rest and during exercise in the heat. *American Journal of Physiology-Regulatory, Integrative and Comparative Physiology* 321, R295-R302 (2021).
- 73 Brimicombe, C. et al. Thermofeel: A python thermal comfort indices library. *SoftwareX* 18, 101005 (2022).
- 74 Liljegren, J. C., Carhart, R. A., Lawday, P., Tschopp, S. & Sharp, R. Modeling the Wet Bulb Globe Temperature Using Standard Meteorological Measurements. *Journal of Occupational and Environmental Hygiene* 5, 645-655 (2008). <https://doi.org/10.1080/15459620802310770>
- 75 Kong, Q. & Huber, M. Explicit Calculations of Wet-Bulb Globe Temperature Compared With Approximations and Why It Matters for Labor Productivity. *Earth's Future* 10, e2021EF002334 (2022). <https://doi.org/https://doi.org/10.1029/2021EF002334>
- 76 Brimicombe, C. et al. Wet Bulb Globe Temperature: Indicating extreme heat risk on a global grid. *GeoHealth* 7, e2022GH000701 (2023).

- 77 Patton, E., Li, W., Ward, A. & Doyle, M. Wet bulb globe temperature from climate model outputs: a method for projecting hourly site-specific values and trends. *International Journal of Biometeorology* (2024). <https://doi.org/10.1007/s00484-024-02776-5>
- 78 Kong, Q. & Huber, M. A new, zero-iteration analytic implementation of wet-bulb globe temperature: development, validation and comparison with other methods. *ESS Open Archive* . (2024). <https://doi.org/10.22541/essoar.171052469.96187535/v1>
- 79 Barton, K. Challenge, promise for nation's "winter salad bowl". *California Agriculture* 51, 4-6 (1997).
- 80 CDFA. California Agricultural Production Statistics. (2023). <<https://www.cdfa.ca.gov/statistics/>>.
- 81 Martin, P. L., Hooker, B., Akhtar, M. & Stockton, M. How many workers are employed in California agriculture? *California Agriculture* 71 (2017).
- 82 Doede, A. L. & DeGuzman, P. B. The disappearing lake: A historical analysis of drought and the Salton Sea in the context of the GeoHealth Framework. *GeoHealth* 4, e2020GH000271 (2020).
- 83 ICPHD. Imperial County Health Status Report (2015-2016). (2016). <https://www.icphd.org/media/managed/medicalproviderresources/HEALTH_STATUS_2015_2016_final.pdf>.
- 84 Farzan, S. F. et al. Assessment of respiratory health symptoms and asthma in children near a drying saline lake. *International Journal of Environmental Research and Public Health* 16, 3828 (2019).
- 85 Heinzerling, A. et al. Risk factors for occupational heat-related illness among California workers, 2000–2017. *American journal of industrial medicine* 63, 1145-1154 (2020).
- 86 Fringer, O. B., Dawson, C. N., He, R., Ralston, D. K. & Zhang, Y. J. The future of coastal and estuarine modeling: Findings from a workshop. *Ocean Modelling* 143, 101458 (2019). <https://doi.org/https://doi.org/10.1016/j.ocemod.2019.101458>
- 87 Bricheno, L. M., Wolf, J. M. & Brown, J. M. Impacts of high resolution model downscaling in coastal regions. *Continental Shelf Research* 34, 7-16 (2014). <https://doi.org/https://doi.org/10.1016/j.csr.2013.11.007>
- 88 NWS. Wet Bulb Globe Temperature Suggested Actions and Impact Prevention, <<https://www.weather.gov/ict/wbgt>> (2023).
- 89 ACGIH. TLV/BEI Guidelines. American Conference of Governmental Hygienists (ACGIH) Threshold Limit Values for Chemical Substances and Physical Agents & Biological Exposure Indices (2017). <<https://www.acgih.org/science/tlv-bei-guidelines/>>.
- 90 Jacklitsch, B. L. et al. Occupational exposure to heat and hot environments: revised criteria 2016. (2016). <<https://www.cdc.gov/niosh/docs/2016-106/default.html>>.
- 91 Wadsworth, G., Riden, H. & Pinkerton, K. Farmer perceptions of climate, adaptation, and management of farmworker risk in California. *Journal of Agriculture, Food Systems, and Community Development* 11, 179–198-179–198 (2022).
- 92 Kamai, E. M. et al. Agricultural burning in Imperial Valley, California and respiratory symptoms in children: A cross-sectional, repeated measures analysis. *Science of The Total Environment* 901, 165854 (2023).
- 93 Qian, Y. et al. Neglecting irrigation contributes to the simulated summertime warm-and-dry bias in the central United States. *npj Climate and Atmospheric Science* 3, 31 (2020). <https://doi.org/10.1038/s41612-020-00135-w>
- 94 Chen, L. & Dirmeyer, P. A. Global observed and modelled impacts of irrigation on surface temperature. *International Journal of Climatology* 39, 2587-2600 (2019). <https://doi.org/https://doi.org/10.1002/joc.5973>
- 95 Liu, J., Jin, J. & Niu, G.-Y. Effects of Irrigation on Seasonal and Annual Temperature and Precipitation over China Simulated by the WRF Model. *Journal of Geophysical Research: Atmospheres* 126, e2020JD034222 (2021). <https://doi.org/https://doi.org/10.1029/2020JD034222>

- 96 Yang, Z. et al. Impact of Irrigation over the California Central Valley on Regional Climate. *Journal of Hydrometeorology* 18, 1341-1357 (2017). <https://doi.org/https://doi.org/10.1175/JHM-D-16-0158.1>
- 97 Orlov, A. et al. Changes in land cover and management affect heat stress and labor capacity. *Earth's Future* 11, e2022EF002909 (2023).
- 98 Baklanov, A. & Zhang, Y. Advances in air quality modeling and forecasting. *Global Transitions* 2, 261-270 (2020).
- 99 Chen, X. et al. Changes in Global and Regional Characteristics of Heat Stress Waves in the 21st Century. *Earth's Future* 8, e2020EF001636 (2020). <https://doi.org/https://doi.org/10.1029/2020EF001636>
- 100 Yang, X., Shen, C., Ullah, I., Curio, J. & Chen, D. Evaluating heat stress and occupational risks in the Southern Himalayas under current and future climates. *npj Climate and Atmospheric Science* 7, 211 (2024). <https://doi.org/10.1038/s41612-024-00764-5>
- 101 Dasgupta, S. et al. Effects of climate change on combined labour productivity and supply: an empirical, multi-model study. *The Lancet Planetary Health* 5, e455-e465 (2021). [https://doi.org/10.1016/S2542-5196\(21\)00170-4](https://doi.org/10.1016/S2542-5196(21)00170-4)
- 102 Yin, J. et al. Global Increases in Lethal Compound Heat Stress: Hydrological Drought Hazards Under Climate Change. *Geophysical Research Letters* 49, e2022GL100880 (2022). <https://doi.org/https://doi.org/10.1029/2022GL100880>
- 103 Zhao, L. et al. Global multi-model projections of local urban climates. *Nature Climate Change* 11, 152-157 (2021). <https://doi.org/10.1038/s41558-020-00958-8>
- 104 Chakraborty, T., Venter, Z. S., Qian, Y. & Lee, X. Lower Urban Humidity Moderates Outdoor Heat Stress. *AGU Advances* 3, e2022AV000729 (2022). <https://doi.org/https://doi.org/10.1029/2022AV000729>
- 105 Vecellio, D. J., Kong, Q., Kenney, W. L. & Huber, M. Greatly enhanced risk to humans as a consequence of empirically determined lower moist heat stress tolerance. *Proceedings of the National Academy of Sciences* 120, e2305427120 (2023). <https://doi.org/doi:10.1073/pnas.2305427120>
- 106 Stull, R. Wet-bulb temperature from relative humidity and air temperature. *Journal of applied meteorology and climatology* 50, 2267-2269 (2011).
- 107 Morris, C. E., Gonzales, R. G., Hodgson, M. J. & Tustin, A. W. Actual and simulated weather data to evaluate wet bulb globe temperature and heat index as alerts for occupational heat-related illness. *Journal of occupational and environmental hygiene* 16, 54-65 (2019).
- 108 Grell, G. A. & Freitas, S. R. A scale and aerosol aware stochastic convective parameterization for weather and air quality modeling. *Atmospheric Chemistry and Physics* 14, 5233-5250 (2014).
- 109 Morrison, H., Thompson, G. & Tatarskii, V. Impact of cloud microphysics on the development of trailing stratiform precipitation in a simulated squall line: Comparison of one-and two-moment schemes. *Monthly weather review* 137, 991-1007 (2009).
- 110 Hong, S.-Y., Noh, Y. & Dudhia, J. A new vertical diffusion package with an explicit treatment of entrainment processes. *Monthly weather review* 134, 2318-2341 (2006).
- 111 Iacono, M. J. et al. Radiative forcing by long-lived greenhouse gases: Calculations with the AER radiative transfer models. *Journal of Geophysical Research: Atmospheres* 113 (2008).
- 112 Jiménez, P. A. et al. A revised scheme for the WRF surface layer formulation. *Monthly weather review* 140, 898-918 (2012).
- 113 He, C. et al. The community Noah-MP land surface modeling system technical description version 5.0. (NCAR Technical Note NCAR/TN-575+ STR, doi: 10.5065/ew8g-yr95, 2023).
- 114 Rasmussen, R. et al. CONUS404: The NCAR-USGS 4-km long-term regional hydroclimate reanalysis over the CONUS. *Bulletin of the American Meteorological Society* 104, E1382-E1408 (2023).

- 115 Broxton, P. D., Zeng, X., Sulla-Menashe, D. & Troch, P. A. A Global Land Cover Climatology Using MODIS Data. *Journal of Applied Meteorology and Climatology* 53, 1593-1605 (2014).
<https://doi.org/https://doi.org/10.1175/JAMC-D-13-0270.1>
- 116 Knyazikhin, Y. J. G., J. L. Privette, Y. Tian, A. Lotsch, Y. Zhang, Y. Wang, J. T. Morisette, P. Votava, R. B. Myneni, R. R. Nemani, S. W. Running. MODIS Leaf Area Index (LAI) and Fraction of Photosynthetically Active Radiation Absorbed by Vegetation (FPAR) Product (MOD15) Algorithm Theoretical Basis Document. (1999).
- 117 Pu, J. et al. Sensor-independent LAI/FPAR CDR: reconstructing a global sensor-independent climate data record of MODIS and VIIRS LAI/FPAR from 2000 to 2022. *Earth System Science Data Discussions* 2023, 1-29 (2023).
- 118 Valayamkunnath, P. Understanding the Role of Vegetation Dynamics and Anthropogenic induced Changes on the Terrestrial Water Cycle, Virginia Tech, (2019).
- 119 Kántor, N. & Unger, J. The most problematic variable in the course of human-biometeorological comfort assessment—the mean radiant temperature. *Central European Journal of Geosciences* 3, 90-100 (2011).
- 120 Di Napoli, C., Hogan, R. J. & Pappenberger, F. Mean radiant temperature from global-scale numerical weather prediction models. *International Journal of Biometeorology* 64, 1233-1245 (2020).
- 121 Jendritzky, G., Menz, G., Schmidt-Kessen, W. & Schirmer, H. Methodik zur raumlichen Bewertung der thermischen Komponente im Bioklima des Menschen (Method for local evaluation of the thermal component of bioclimate of people). Hannover, Akademie fur Raumforschung und Landesplanung (1990).
- 122 Staiger, H. & Matzarakis, A. in *Proceedings of the 7th Conference on Biometeorology*. Freiburg: Albert-Ludwigs-University of Freiburg. 213-218.
- 123 De Dear, R. Ping-pong globe thermometers for mean radiant temperatures. *H and V Engineer* 60, 10-11 (1988).
- 124 Guo, H., Teitelbaum, E., Houchois, N., Bozlar, M. & Meggers, F. Revisiting the use of globe thermometers to estimate radiant temperature in studies of heating and ventilation. *Energy and Buildings* 180, 83-94 (2018).
- 125 Thorsson, S., Lindberg, F., Eliasson, I. & Holmer, B. Different methods for estimating the mean radiant temperature in an outdoor urban setting. *International Journal of Climatology* 27, 1983-1993 (2007).
<https://doi.org/https://doi.org/10.1002/joc.1537>